





## Inline cryogenically cooled radio-frequency ion trap as a universal injector for cold ions into an electrostatic ion-beam storage ring: Probing and modeling the dynamics of rotational cooling of $\text{OH}^-$

H. B. Pedersen ,\* H. Juul , F. K. Mikkelsen, A. P. Rasmussen , and L. H. Andersen   
*Department of Physics and Astronomy, Aarhus University, DK-8000 Aarhus C, Denmark*



(Received 22 September 2022; accepted 31 October 2022; published 18 November 2022)

We describe the setup and characterization of a cryogenic multipole radio-frequency (RF) ion trap that enables the accumulation and cooling of mass-selected ions before injection into the SAPHIRA storage ring. To characterize the RF trap setup, we use  $\text{OH}^-$  anions and explore the threshold photodetachment cross section measured after storage in SAPHIRA as a probe of the rotational temperature. Beyond the temperature of the ion trap assembly, cooled to 6 K, the final rotational temperature of the  $\text{OH}^-$  ions is strongly influenced by the density of cooled He and the actual number of trapped ions while much less affected (possibly unaffected) by the time-varying field of the trap. To obtain rotationally cold  $\text{OH}^-$  ions, the RF trap must be operated with low He density and a low number of ions. High He densities, corresponding to a strong coupling of the trapped ions and He gas, lead to a significant rotational heating of the trapped ion ensemble, and the He density seems to limit the actual reachable rotational temperature. We demonstrate that cold ions in the RF trap remain cold for at least 30 ms in the SAPHIRA (300 K) storage ring at a base pressure of  $\sim 8 \times 10^{-9}$  mbar.

DOI: [10.1103/PhysRevA.106.053111](https://doi.org/10.1103/PhysRevA.106.053111)

### I. INTRODUCTION

For more than two decades, electrostatic storage devices in the form of linear ion-beam traps [1–8] and storage rings [9–18] have been important devices for research in several areas of atomic and molecular physics. The trapping of fast ion beams in electrostatic fields benefits from being mass-independent and allows for compact and flexible setups while they are realistically limited to beam energies in the keV region as compared to magnetic storage rings where MeV beams can be accommodated. The storage of fast ions under high and ultrahigh vacuum conditions, independent of the principle of storage (electrostatic or magnetic), gives advantageous experimental possibilities as for example long storage time prior to experiments, long observation times after interrogation, e.g., by photoabsorption, and essentially universal access to neutral fragments, charged fragments, and electrons, as well as light emitted from stored ions.

One central challenge to experiments in electrostatic storage devices with atomic and molecular ions is to control their internal energy both initially (before injection) and during storage where the internal state of the ions can develop due to inelastic collisions with the rest gas in the vacuum system, ion-ion collisions, interactions with the ambient radiation field at the instrument temperature, and interactions with the applied trapping fields. This has for instance proven important for studies of the lifetime of very weakly bound systems [19–23], for understanding spontaneous internal dynamics of molecules [24–28] and for probing complex molecules [29]

Cooling of the entire ion storage setup, i.e., aiming to control the effect of the ambient radiation field on the internal energy distribution of the ions and lower the density of the residual gas, were first done with liquid nitrogen in storage rings [11,19,24]. Cooling of entire instruments to cryogenic temperatures have been done in both linear ion-beam traps [4,6,20] and in storage rings [14,17,18]. As the cold environments in these devices additionally lead to very low residual gas densities, the ion storage times can be extremely long ( $\sim$  hours) whereby molecular systems with allowed optical transitions can cool by spontaneous emission of radiation [30–33], however, at the cost of very low experimental duty cycles.

The actual internal temperature of the stored fast ions has been diagnosed for small molecules by probing directly the distribution of rotational states by photodissociation [34] or photodetachment [31,32]. For larger molecules the internal energy has been diagnosed by observing changes in their decay dynamics as well as induced decay changes in the response to photoabsorption [25–29] as a function of time after storage, i.e., linking the nature of photoelectrons or photofragments to the internal temperature.

The addition of multipole radio frequency (RF) ion traps [35] as an integral part of the ion preparation both at room temperature [36], liquid nitrogen temperature [37–39] and cryogenic temperatures [40–42] have facilitated ion accumulation and initial cooling of ions prior to experiments in electrostatic storage devices.

In this paper, we describe the construction and commissioning of an cryogenically cooled 16-pole RF trap as accumulator and injector of cold ions into the (room-temperature) storage ring SAPHIRA [15]. The RF trap is installed in an inline geometry on the injection line towards SAPHIRA, i.e., at a location with ultra high vacuum

\*Corresponding author: [hbp@phys.au.dk](mailto:hbp@phys.au.dk)

conditions and where initial magnetic mass selection of ions from a fast ion beam has been performed.

Generally, the use of multipole RF traps is very versatile for the purpose of accumulation and cooling of ions [43–46] since they are small and they are easily cooled either by liquid nitrogen or via cryogenic stages. By controlled inlet of gas (often He) into the cooled trap, the neutral (He) gas thermalizes to the trap temperature, and consequently, as the trapped ions are brought in collisional contact with the cold gas, the ensemble of ions will tend to thermalize both their translational motion and their internal energy to the temperature of the cold gas. The actual measurement of the resulting translational temperature of trapped ions have been done by observing the Doppler broadening of rotational lines [47–50], while the internal rotational temperature has been deduced from direct measurements of rotational state populations as probed by photofragmentation [47] or photodetachment [51,52].

For an ensemble of ions trapped in a multipole RF trap, it is a general observation that the actual temperatures (translational and internal) of the ensemble are higher than the temperature of the inlet gas [53]. For example, for small positive ions, Mikosch *et al.* [47] used a trap at 55 K, while observing translational and rotational temperatures of  $\text{H}_3^+$  on the order of 150 K. Asvany *et al.* [48,49] reported translational temperatures of approximately 10 K in excess of the gas temperature for  $\text{H}_2\text{D}^+$  and  $\text{D}_2\text{H}^+$ . Similarly, for negative ions, Otto *et al.* [51] and Hauser *et al.* [52] found rotational temperatures in excess of the trap temperature, being 10–20 K for trap temperatures below 30 K, leaving the final reachable temperature on the order of 25 K.

For the commissioning of the RF trap and storage ring combination described in the present paper, we use  $\text{OH}^-$  anions and the measured photodetachment cross section near threshold as a probe of the rotational distribution [31,32,51]. We also encounter the discrepancy between the trap temperature and the actual rotational temperature of the extracted ions. Experimentally, we observe a correlation between this discrepancy and both the number of trapped ions and importantly also the density of the He-buffer gas, where both (number of ions and He density) need to be low to obtain the coldest ions. We suggest that the reason for these observations lie in the strength of the coupling between the trapped ions themselves as well as between the ions and the He-buffer gas. The coupling strength can for example be quantified by the number of collisions during a round trip in the trap. A weak coupling with  $< 1$  collision per round trip, allows cooling as collisions will preferentially take place at locations of low energy (high cross section), while a stronger coupling with  $\gg 1$  collision per round trip will oppositely force the wider span of collision energies available throughout the trap to be probed, which will lead to an ion temperature in significant excess of the buffer gas temperature.

In Sec. II we describe the experimental RF trap, and in Sec. V we present the characterization of the complete experimental system with RF trap, ion storage ring, and laser photodetachment. In between these sections, we provide explicit explanations of the data evaluation and the background for the interpretation of the obtained results. Thus, in Sec. III we give a complete account of the model for threshold photodetachment of  $\text{OH}^-$ , and in Sec. IV we outline an explicit

framework for numerical simulations on the ion dynamics in the multipole RF trap, including collisions and space-charge effects.

## II. EXPERIMENT

### A. Overview of the experiment

Figure 1 shows schematically the used setup in the present experiments, and Fig. 2 shows a layout of the timing scheme employed. Briefly, negative ions are produced in a Cs sputter ion source [54] using an Al cathode with an insert of pressed Cu powder which in combination with gaseous species in the residual gas inside the ion source (likely  $\text{H}_2$ ,  $\text{O}_2$ , or  $\text{H}_2\text{O}$ ) produces  $\text{OH}^-$  anions. A fast beam of negative ions of charge  $q_i = -e$  are extracted from the source and accelerated to a final kinetic energy of  $E_i = 4$  keV. The ion beam is passed through a magnetic field to obtain a beam composed of mass  $m_i = 17$  amu ions (here mainly containing  $\text{OH}^-$  with a small trace of  $^{17}\text{O}^-$ ) with an integral current of 4–8 nA.

Using a switchable potential on a parallel plate deflector (beam chopper), a pulse of the beam with a selectable temporal length  $T_{\text{INJ}}$  ( $\mu\text{s}$ -s) is allowed to pass farther into the beamline. This beam pulse is sent towards the radio frequency trap (see Sec. II B for a detailed description), which is biased to a potential of  $V_{\text{TRAP}} \sim -4$  kV, and the incoming ions are decelerated and trapped in the RF trap for a selectable time  $T_{\text{COOL}}$  ( $\mu\text{s}$ -s). The trapping is accomplished by radial confinement in a time-varying potential and axial confinement via static, but switchable, potentials on electrodes at the entrance and exit sides of the trap [35]. The trap can be cooled to cryogenic temperatures and cooled He gas can be lead directly into the trapping volume. To extract the ions, potentials on the exit side of the trap are lowered for a time  $T_{\text{OP}}$  ( $\sim 20$   $\mu\text{s}$  for  $\text{OH}^-$ ) so the ions are re-accelerated to 4 keV kinetic energy and injected into the SAPHIRA storage ring during a transfer period  $T_{\text{TR}}$  ( $\sim 30$   $\mu\text{s}$  for  $\text{OH}^-$ ) and stored for an adjustable time  $T_{\text{RING}}$  (ms-s). After a period  $T_{\text{L}}$  of ion storage in SAPHIRA, a laser pulse with a width of a few ns from a tunable laser (EKSPLA NT342) can be send into one of the arms of the SAPHIRA storage ring where it, for the present experiment, intercepts the ion beam in a merged beams geometry.

Neutral fragments (OH, O, or H) generated in collisions with the residual gas in the storage ring are monitored with microchannel plate detectors (DET1 and DET2) situated behind the first and fourth corner of SAPHIRA, where for the present experiment, a version of DET2 with a central hole of diameter 10 mm is applied. The neutral fragments (OH) produced by laser photodetachment are registered with DET2. The central hole in this detector (DET2) allows passage of the laser pulse while a significant part of the photofragments impacts on the detector. The intensity of the laser pulse ( $\sim 0.5$  mJ/pulse) is monitored with a power meter after the passage through the storage ring.

### B. Mechanical and electrical setup of the radio-frequency trap

Figure 3 gives an impression of the basic elements of the RF trap, including the electrode stacks on the entrance and exit sides that facilitate the ion injection and extraction, and outlines the electrical setup applied to operate the trap. An

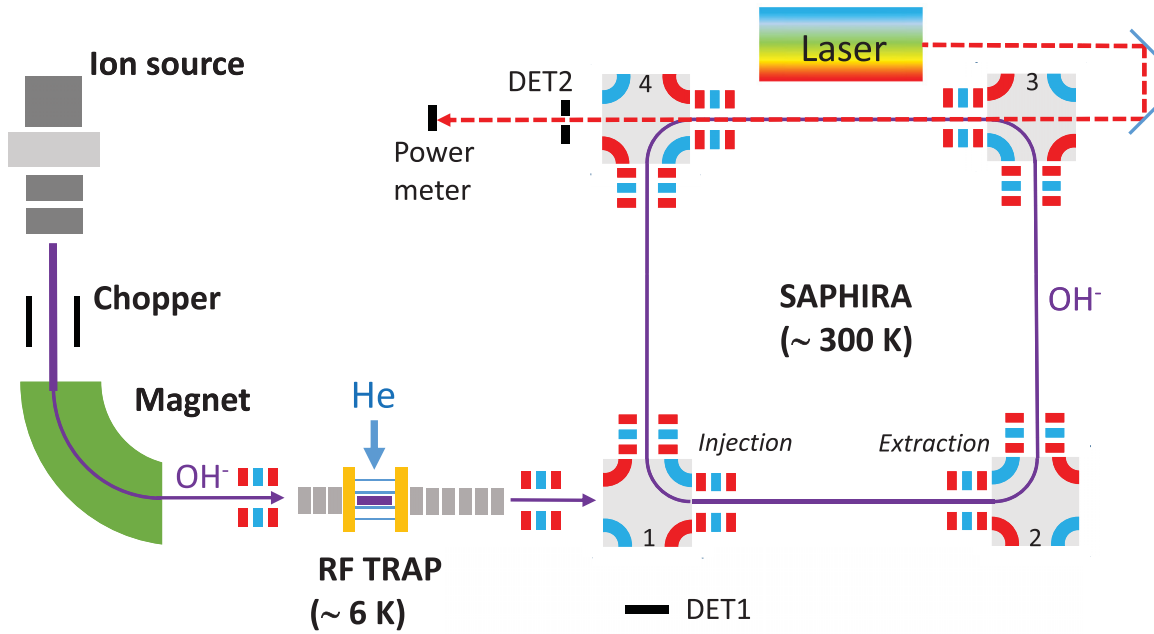


FIG. 1. Overview of the experimental setup showing the ion source from which a  $E_i = 4$  keV fast ion beam is extracted, the magnet used for ion-mass selection, the cryogenic 16-pole radio-frequency trap, where ions are accumulated and cooled, the SAPHIRA storage ring [15], and the pulsed (ns) tunable laser used to induce photodetachment of stored  $\text{OH}^-$  ions in a near merged beam geometry. Fragments exiting the storage ring due to neutralization in the residual gas are detected with the two detectors labeled DET1 and DET2. Fragments from laser photodetachment are additionally detected on DET2, which has a central hole that allows passage of the laser to a power meter.

exploded drawing of the central part of trap assembly on the cryo-cooler is shown in Fig. 4.

The electrode stack on the entrance side is composed of six cylindrical electrodes of length 9 mm and 6 mm inner

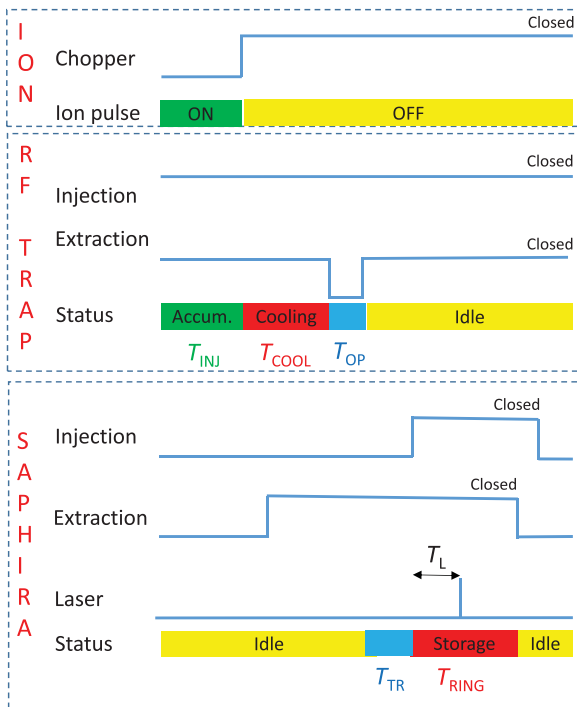


FIG. 2. Experimental timing scheme used for the present experiments indicating the operation the ion pulsing, the trapping in the RF trap, and the storage in SAPHIRA.

diameter and with a distance of 3 mm between neighboring electrodes. The electrode stack on the exit side is similarly composed of 14 electrodes. For the present investigation, the electrodes are coupled together as depicted in Fig. 3, i.e., one potential is used for the injection stack, and three potentials for the extraction stack, however, the design is intentionally kept flexible to easily allow different injection or extraction schemes.

The ion trap is composed of 16 cylindrical poles of 1 mm diameter of length 43 mm hold equidistantly on a radius of  $r_0 = 5$  mm and two sets of cap electrodes (same dimensions as the electrodes used on the entrance and exit stacks) on both the entrance and exit side and positioned partly inside the cylindrical enclosure defined by the rods. The distance between the innermost set of cap electrodes is  $L_0 = 32.5$  mm.

The complete RF trap assembly is biased to a potential of  $V_{\text{TRAP}} (\sim E_i/q_i = -4$  kV) relative to ground so ions in the fast beam are decelerated upon entry into the trap region. During deceleration and injection, the ion trajectories into the trap are affected by a focusing field defined by the potential  $V_E (\sim 2$  kV). Similarly, during the re-acceleration following the period of ion cooling, the ions are affected by the potentials  $V_{X1} (\sim 2.4$  kV),  $V_{X2} (\sim 1$  kV), and  $V_{X3} (\sim 1.8$  kV).

The rods of the trap assembly are connected to a  $f_{\text{RF}} = 4$  MHz radio frequency power supply with adjustable amplitude  $V_{\text{RF}}$  (0–750 V). The potentials ( $V_{\text{CE1}}$ ,  $V_{\text{CE2}}$ ,  $V_{\text{CX1}}$ , and  $V_{\text{CX2}}$ ) applied to each cap electrode can be rapidly switched (rise and fall time  $\sim 50$  ns) between lower and higher levels which are each adjustable within  $\pm 200$  V.

The central parts of the trap assembly, i.e., the 16 poles with RF potentials and the end cap electrodes (see Fig. 4), are placed inside a Cu house that is mounted directly on

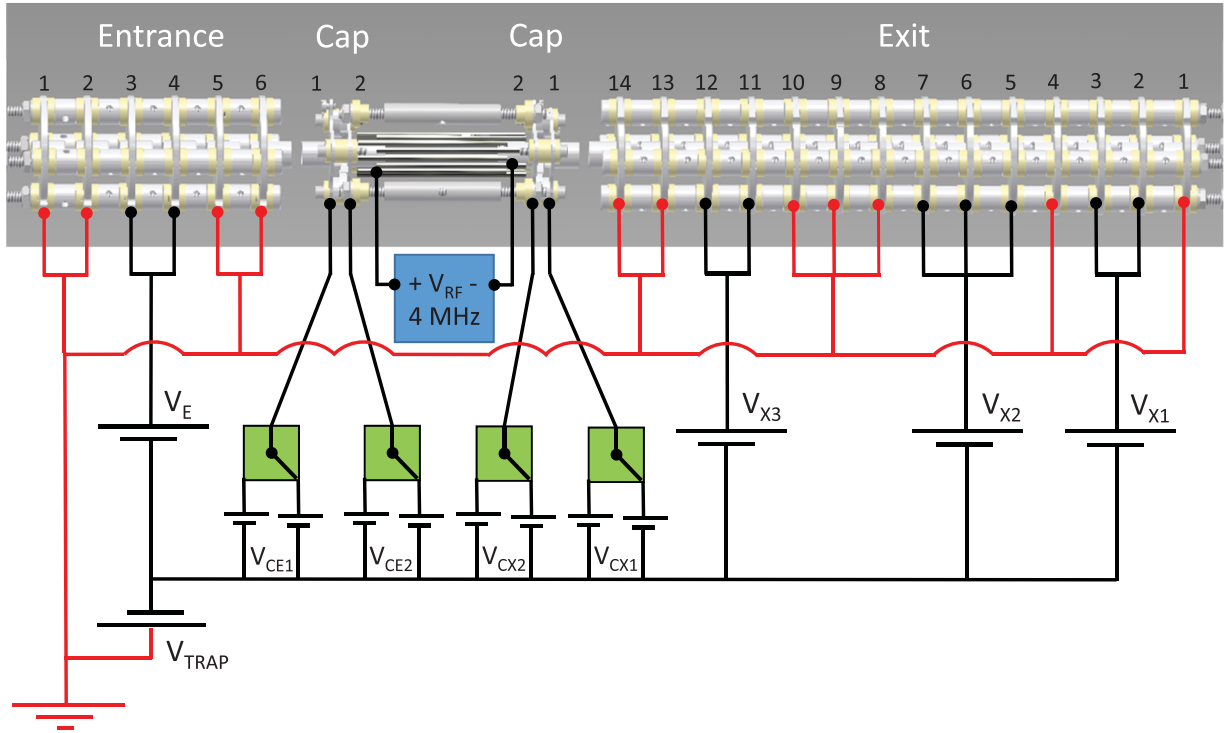


FIG. 3. Impression of the construction of the trap and the electrical setup during operation in this study. The ion trap has 16 poles on time-varying potentials (amplitude  $V_{RF}$  and frequency  $f_{RF}$ ) that provides radial stability and two sets of end cap electrodes on switchable potentials at the entrance ( $V_{CE1}$  and  $V_{CE2}$ ) and exit ( $V_{CX1}$  and  $V_{CX2}$ ) sides of the trap. The electrode stack (labeled 1–6) on the entrance of the trap facilitates deceleration and injection of an initially fast ion beam from the ion source, and correspondingly, the stack on the exit side (labeled 1–14) enables reacceleration of the ions into a confined pulse that can be injected into SAPHIRA (see Fig. 1).

the second stage (nominally 4 K) on a cryo-cooler (Sumitomo, model PR-082B) separated by four thin sheets (area  $40 \times 40 \text{ mm}^2$  and thickness 0.5 mm) of sapphire crystals to provide electric insulation between the trap assembly (on high voltage,  $V_{TRAP}$ ) and the cooling stage (ground potential) while still maintaining good thermal contact.

The temperature of the second stage of the cryo-cooler is monitored directly with a silicon diode sensor (Lake Shore, model DT-670B-SD) and the actually measured temperature of this stage was  $T_{cryo} \sim 6 \text{ K}$  during operation. The cooling of

the trap assembly from 300 K to 6 K is completed in a few hours while the heating to room temperature takes approximately one day under the present conditions.

### C. Vacuum conditions and He-buffer gas density

The RF trap is mounted inside a vacuum chamber that can be pumped to a residual pressure of  $\sim 5 \times 10^{-9}$  mbar by turbo pumps. He-buffer gas is supplied to the chamber through a leak valve at room temperature with an external pressure (on the entrance side of the leak valve) of He of approximately 1.5 bar. Following the leak valve, the He gas is guided through a Cu tube that is wound eight times around and closely attached to the first (40 K) stage of the cryo-cooler. Thereafter, the He gas is guided into the trap assembly through a port on the trap enclosure that ensures good contact between the gas and trap body before the cooled gas actually enters the ion trap volume.

The pressure in the vacuum chamber that holds the ion trap  $p_{CH}$  is monitored at room temperature with an ionization gauge (Pfeiffer, model PKR251). A correction of  $f_{He} = 5.9$  is applied for correcting the direct reading of the He pressure. In the present experiments, the He pressure as monitored in the surrounding chamber is varied in the range  $p_{CH} \sim (0.3\text{--}6) \times 10^{-5}$  mbar [i.e., with direct readings on the gauge in the range  $p_{gauge} \sim p_{CH}/f_{He} = (0.5\text{--}10) \times 10^{-6}$  mbar]. The corresponding pressure in the SAPHIRA storage ring  $p_{RING}$  becomes  $\sim 1.6 \times 10^{-4} \times p_{CH} + 7.1 \times 10^{-9}$  mbar, which demonstrates a very good, but measurable,

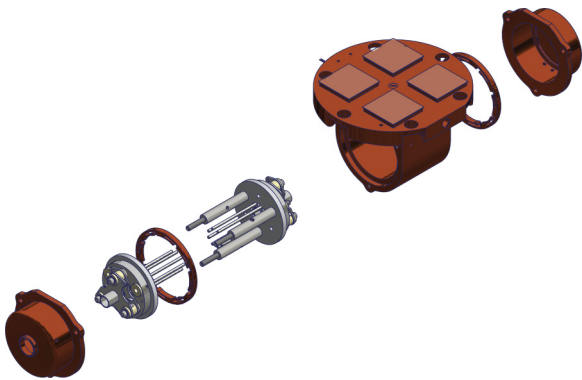


FIG. 4. Exploded view of the central part of the RF trap assembly that is cooled by the second stage of the cryo-cooler. The contact to the second stage of the cryo-cooler is made through four sheets of thermally conducting and electrically insulating sapphire plates as indicated on top of the central Cu house.

vacuum separation between the chamber holding the ion trap and the SAPHIRA vacuum system.

The density of He atoms in the vacuum chamber that holds the RF trap assembly can be well represented as an ideal gas with density  $n_{\text{CH}} = p_{\text{CH}}/k_B T_{\text{CH}}$  where the chamber temperature is  $T_{\text{CH}} = 300$  K. For a pressure of  $p_{\text{CH}} = 5.0 \times 10^{-6}$  mbar the corresponding density is hence  $n_{\text{CH}} = 1.2 \times 10^{11}$  cm $^{-3}$ .

A central quantity for the characterization of the RF trap is the actual density  $n_{\text{He}}$  of He gas inside the RF trap where ions are trapped. To estimate how this density is related to the density of He gas outside the trap assembly ( $n_{\text{CH}}$ ), we consider the motion of a gas in an imaginary rectangular box of length  $L_x = 80$  mm and cross sectional area  $L_y \times L_z = 5.3 \times 5.3$  mm $^2$ , corresponding roughly to the volume from which gas can leak out of the Cu house with the RF trap (see Fig. 4) into the surrounding vacuum chamber. The He gas in this volume is at temperature  $T_{\text{He}}$  and the distribution of velocities  $v_\alpha$  in each dimension  $\alpha$  ( $= x, y, z$ ) is given by

$$f(v_\alpha, T_{\text{He}}) = \sqrt{\frac{m_{\text{He}}}{2\pi k_B T_{\text{He}}}} \exp\left(\frac{-m_{\text{He}} v_\alpha^2}{2k_B T_{\text{He}}}\right). \quad (1)$$

The He gas is considered at sufficiently low density so the mean free path of a He atom is much larger than the dimension (80 mm) of the cylinder; at a pressure of  $10^{-5}$  mbar and a temperature of 10 K, the mean free path of a He atom is on the order of  $3 \times 10^3$  mm.

To estimate the leakage of He atoms out of the imaginary box from a specific point  $(x, y, z)$  inside the box, we assume that the condition of an atom to escape the box is that its velocities allow a direct motion through the openings of the box ends at  $x = \pm L_x/2$ . Thus, if we consider a He atom at location  $x$  and moving with a positive velocity in the  $x$  direction ( $v_x > 0$ ) it will potentially reach the exit at  $x = +L_x/2$  after a time  $\Delta t_x = (L_x/2 - x)/v_x$ , and it will escape the volume if its corresponding  $y$  or  $z$  coordinates do not exceed the radial openings at  $y = \pm L_y/2$  and  $z = \pm L_z/2$ . The fraction  $P_+(x, y, z, T_{\text{He}})$  of He gas that escapes the box through the opening at  $x = +L_x/2$  from the point  $(x, y, z)$  inside the volume can then be estimated as

$$\begin{aligned} P_+(x, y, z, T_{\text{He}}) &= \int_0^\infty dv_x f(v_x, T_{\text{He}}) \\ &\times \int_{-(L_y/2-y)/\Delta t_x}^{(L_y/2+y)/\Delta t_x} dv_y f(v_y, T_{\text{He}}) \\ &\times \int_{-(L_z/2-z)/\Delta t_x}^{(L_z/2+z)/\Delta t_x} dv_z f(v_z, T_{\text{He}}), \quad (2) \end{aligned}$$

and a similar expression can be established for the fraction of gas  $P_-(x, y, z, T_{\text{He}})$  that escapes through the opening at  $x = -L_x/2$ . The total fraction of gas leaking out of the imaginary volume can then be estimated by averaging over points in the entire box:

$$\begin{aligned} f_i(T_{\text{He}}) &= \frac{1}{L_x L_y L_z} \int P_+(x, y, z, T_{\text{He}}) \\ &+ P_-(x, y, z, T_{\text{He}}) dx dy dz. \quad (3) \end{aligned}$$

By numerical integration, we explicitly obtain  $f_i(10 \text{ K}) = 0.028$  and  $f_i(300 \text{ K}) = 0.024$ . To summarize, the He gas density inside ( $n_{\text{He}}$ ) and outside ( $n_{\text{CH}}$ ) the RF trap assembly are approximately related as

$$\begin{aligned} n_{\text{He}}(T_{\text{He}}) &= f_i(T_{\text{He}}) \times n_{\text{CH}} \\ &= f_i(T_{\text{He}}) \times \frac{p_{\text{CH}}}{k_B T_{\text{CH}}} \\ &= f_i(T_{\text{He}}) \times f_{\text{He}} \times \frac{p_{\text{gauge}}}{k_B T_{\text{CH}}}. \quad (4) \end{aligned}$$

### III. MODEL FOR THRESHOLD PHOTODETACHMENT OF OH $^-$

#### A. General formalism

The threshold photodetachment of OH $^-$  has been studied in a number of experiments [55,59–64] and in theory [65]. In recent studies with an RF trap [51] and with cryogenic storage rings [31,32], measurements of the threshold photodetachment cross section were applied to probe the rotational temperature of the ensemble of trapped or stored ions.

In this study, we similarly follow the strategy to infer the rotational temperature of stored OH $^-$  ion in SAPHIRA after cooling the ions in the RF trap by measurement of the threshold photodetachment cross section. Although the formalism of this modeling has been given before [31,32,51,59,62], there are significant differences between the descriptions. For example, the dependence of the centrifugal term on the quantum number for angular momentum of the rotational energy for OH as obtained from the original analysis in Ref. [57] is different in Ref. [59] and Ref. [31], and there are substantial disagreements on the actual implementation of the rotational intensity factors across the applied models. We follow the formalism described in the recent analysis provided by Meyer *et al.* [31] where in particular the formulas for the rotational intensity factors were carefully revised.

The rotational structure of OH $^-$  and OH as well as the transitions leading to s-wave photodetachment of OH $^-$  near threshold are illustrated schematically in Fig. 5. The ground  $^2\Sigma^+$  electronic state of OH $^-$  has a rotational structure characterized by integer rotational quantum numbers  $J$  ( $= N$ ) (often labeled  $J''$ , but here we choose  $J$  to simplify the notation), and parity  $(-1)^J$ . The electronic ground state of OH is split by spin-orbit coupling into a  $^2\Pi_{3/2}$  state with levels denoted  $F_1$ , and a  $^2\Pi_{1/2}$  state with levels denoted  $F_2$ . The resulting energy levels in each state ( $F_1$  or  $F_2$ ) are characterized by a pure rotational quantum number  $N'$ , a half integer quantum number  $J'$  for the total angular momentum, and a label  $e$  or  $f$  reflecting the parity; the  $e$  states have parity  $p_e = (-1)^{J'-1/2}$ , and the  $f$  states have parity  $p_f = -(-1)^{J'-1/2}$ .

For s-wave photodetachment, the connected OH $^-$  state and OH state must have opposite parity, and transitions with  $J' - J = \pm 1/2$  and  $J' - J = \pm 3/2$  are allowed. The transitions are labeled as  $\beta = \Delta N 2\Omega'(J)$ , where  $\Delta N = N' - N = \text{O, P, Q, R, or S}$  (corresponding to values  $-2, -1, 0, 1, \text{ or } 2$ ) is the resulting difference in pure rotational quantum numbers,  $2\Omega'$  names the states  $F_1$  (with  $2\Omega' = 3$ ) or  $F_2$  (with  $2\Omega' = 1$ ), and  $J$  is the initial rotational quantum number of the OH $^-$  level.

In thermal equilibrium at a temperature  $T_R$ , the population of the rotational levels of OH $^-$  with quantum number  $J$  is

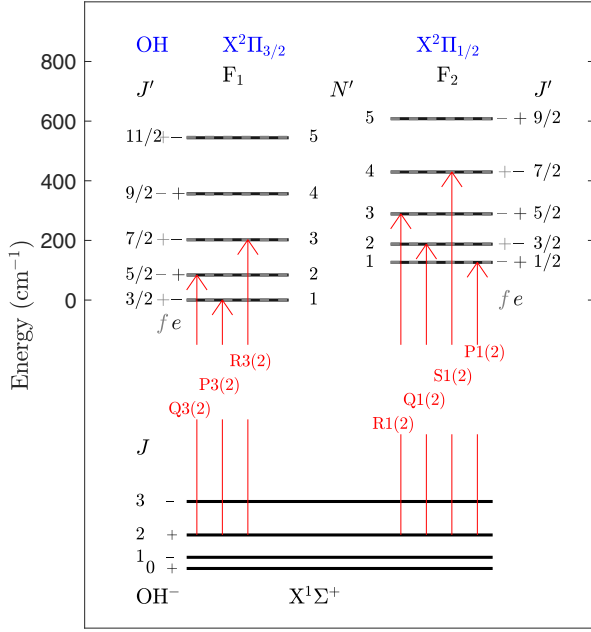


FIG. 5. Rotational transitions from the  $X^1\Sigma^+$  ground state of  $\text{OH}^-$  to the two  $\Lambda$ -doublet  $^2\Pi$  states of OH (inspired by Fig. 2 in Ref. [55]). The dark gray line of the OH molecular states indicates the  $e$ -level and the dashed light gray lines the  $f$  level, and the corresponding parities ( $\pm$ ) are given with dark and light gray. The energies has been calculated with rotational parameters for  $\text{OH}^-$  given in Ref. [55], rotational and spin-orbit coupling parameters for OH given in [56], and using the formalism applied in [31,57,58].

given by

$$p_J = \frac{1}{Z}(2J+1)\exp\left(\frac{-E_J^{\text{OH}^-}}{k_B T_R}\right), \quad (5)$$

where  $E_J^{\text{OH}^-}$  is the energy of the rotational level of  $\text{OH}^-$  and  $Z$  is a normalization constant ensuring  $\sum_J p_J = 1$ .

For a particular rotational transition from a rotational level  $J$  of  $\text{OH}^-$  to a level  $J'$  of OH, the photodetachment cross section near threshold can be written as

$$\sigma_\beta(E_\gamma) = \sigma_0 \times \frac{I_\beta}{2J+1} \times (E_\gamma - E_\beta^{\text{th}})^{p_\beta}, \quad E_\gamma \geq E_\beta^{\text{th}}, \quad (6)$$

where  $\sigma_0$  represents the amplitude of the cross section,  $I_\beta$  is a rotational intensity factor [31,61,64],  $E_\beta^{\text{th}}$  is the threshold energy for the transition, and where the photon energy dependence has been assumed to be given as a power law with an exponent  $p_\beta$ . This exponent was deduced to be  $p_\beta = 0.28$  [61,65] from fits to detachment spectra obtained under warm conditions and to be smaller in recent fit to spectra at cold conditions [51]. The data presented in Sec. VB from the present work are best represented with a value of  $p_\beta = 0.2$ . It should be noted that another energy dependence of the detachment cross section was applied by Meyer *et al.* [31], however, the difference between this and the one used here is insignificant for the purpose of fit near threshold. The explicit form of the transition thresholds energies and intensity factors are given in Sec. III B and Sec. III C, respectively.

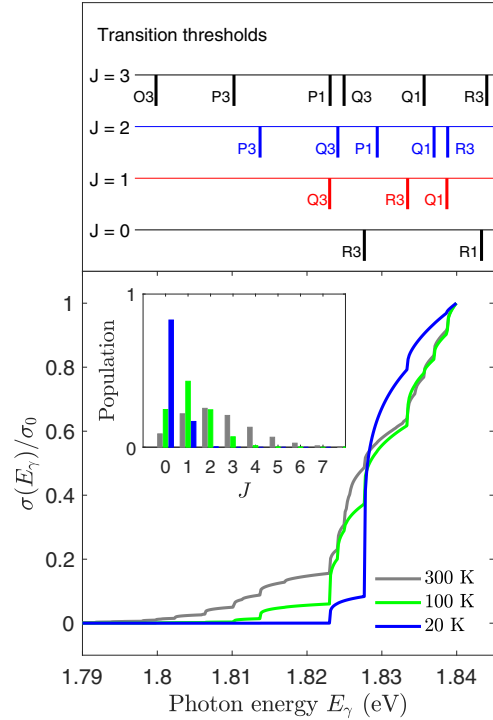


FIG. 6. Illustration of the threshold photodetachment cross section of  $\text{OH}^-$ . The upper panel displays schematically the energetic location of the thresholds for transitions (see text and Fig. 5) where, however, the parentheses giving the value of  $J$ , the initial rotational quantum number of  $\text{OH}^-$ , have been omitted. The lower panel shows model cross sections as defined in Eq. (7) for three different temperatures and normalized to the cross section value at  $E_\gamma = 1.84$  eV. The level populations corresponding to the applied temperatures [Eq. (5)] are shown in the insert.

The total effective photodetachment cross section at a rotational temperature  $T_R$  can be written as

$$\sigma(E_\gamma) = \sum_\beta p_J \times \sigma_\beta(E_\gamma) + \sigma_B, \quad (7)$$

where the sum is over all allowed transitions. An extra term  $\sigma_B$  is added to the formula to represent a background in the experiment stemming from impurities in the  $\text{OH}^-$  beam: in the present case a small fraction of  $^{17}\text{O}^-$  is found. Equation (7) thus constitutes the final relation we use to model the experimentally obtained cross sections. In Fig. 6 we show an explicit illustration of the model cross section as calculated for three different rotational temperatures. Clearly, as also explored in previous measurements [31,32,51], the threshold photodetachment cross section allows a sensitive way to determine the rotational temperature as the various rotational thresholds gives rise to very distinct features in the cross section.

## B. Energies levels of OH and $\text{OH}^-$

Following Meyer *et al.* [31], the energies of the rotational levels of  $\text{OH}^-$  can be obtained as

$$E_J^{\text{OH}^-} = B_0^{\text{OH}^-} J(J+1) - D_0^{\text{OH}^-} J^2(J+1)^2, \quad (8)$$

where the rotational constants are  $B_0^{\text{OH}^-} = 18.741 \text{ cm}^{-1}$  and  $D_0^{\text{OH}^-} = 2.052 \times 10^{-3} \text{ cm}^{-1}$  as determined in a study of threshold photodetachment [55].

To evaluate the energies of the rotational levels of OH, one defines the parameter

$$X_{J'} = \sqrt{4(J' + 1)^2 + Y(Y + 1)}, \quad (9)$$

where the coupling parameter  $Y = A_0^{\text{OH}}/B_0^{\text{OH}} = -7.5030$ , is the ratio of the spin-orbit coupling constant  $A_0^{\text{OH}} = -139.18 \text{ cm}^{-1}$  and the rotational constant  $B_0^{\text{OH}} = 18.550 \text{ cm}^{-1}$  [56] for the OH molecule.

The energy for the F1 and F2 levels can be obtained as

$$E_{J',F1}^{\text{OH}} = B_0^{\text{OH}}[(J' + 1/2)^2 - 1 - X/2] - D_0^{\text{OH}}J'^4 + p_{e/f}\Delta E_{F1,ef}, \quad (10)$$

$$E_{J',F2,f/e}^{\text{OH}} = B_0^{\text{OH}}[(J' + 1/2)^2 - 1 + X/2] - D_0^{\text{OH}}(J' + 1)^4 + p_{e/f}\Delta E_{F2,ef}, \quad (11)$$

where the parities are  $p_e = (-1)^{j'-1/2}$  and  $p_f = -(-1)^{j'-1/2}$  and where the energy splitting of the  $e$  and  $f$  states are given by

$$\Delta E_{F1,fe} = -(J'+1/2)\{(-1/2+2/X - y/X)[P_0/2 + Q_0(0)] + 2Q_0(0)(J'+1/2)(J'+3/2)/X\} \quad (12)$$

and

$$\Delta E_{F2,fe} = (J'+1/2)\{(1/2 + 2/X - Y/X)[P_0/2 + Q_0(0)] + 2Q_0(0)(J'+1/2)(J'+3/2)/X\}. \quad (13)$$

The molecular constants in these formulas are explicitly  $B_0^{\text{OH}} = 18.550 \text{ cm}^{-1}$ ,  $D_0^{\text{OH}} = 1.916 \times 10^{-3} \text{ cm}^{-1}$ ,  $P(0) = 0.234 \text{ cm}^{-1}$ , and  $Q_0(0) = -0.039 \text{ cm}^{-1}$  [56].

The electron affinity of  $\text{OH}^-$  is  $E_{\text{EA}}^{\text{OH}^-} = 14741.0 \text{ cm}^{-1}$  [64] corresponding to the transition R3(0). Hence, the transition threshold energy for a given transition  $\beta$  can be obtained as

$$E_\beta = E_{J',F_x}^{\text{OH}} - E_{0,F1}^{\text{OH}} + E_{\text{EA}}^{\text{OH}^-} - E_J^{\text{OH}^-}. \quad (14)$$

### C. Rotational intensity factors $I_\beta$

To compute the rotational intensity factors  $I_\beta$ , one first defines the mixing coefficient

$$\kappa_{J'} = \left( \frac{X_{J'} - 2 + Y}{2X} \right)^{1/2} \quad (15)$$

and the state amplitudes [31] for the F1 states

$$c_1^{\text{F1}} = \kappa_{J'}, \quad c_2^{\text{F1}} = -\sqrt{1 - \kappa_{J'}^2} \quad (16)$$

and the F2 states

$$c_1^{\text{F2}} = \sqrt{1 - \kappa_{J'}^2}, \quad c_2^{\text{F2}} = \kappa_{J'}. \quad (17)$$

With these parameters, the rotational intensity factors are explicitly given as follows [64]: For the O3 and P1 branch ( $J' - J = -3/2$ )

$$I_{O3/P1(J)} = \frac{J-1}{2(2J-1)} \times (c_1^{\text{F1/F2}}\sqrt{J} + c_2^{\text{F1/F2}}\sqrt{J-2})^2, \quad (18)$$

for the P3 and Q1 branch ( $J' - J = -1/2$ )

$$I_{P3/Q1(J)} = \frac{J-1}{2(2J-1)} \times (c_1^{\text{F1/F2}}\sqrt{J-1} - c_2^{\text{F1/F2}}\sqrt{J+1})^2 + \frac{1}{2}(c_1^{\text{F1/F2}}\sqrt{J+1} + c_2^{\text{F1/F2}}\sqrt{J-1})^2, \quad (19)$$

for the Q3 and R1 branch ( $J' - J = +1/2$ )

$$I_{Q3/R1(J)} = \frac{J+2}{2(2J+3)} \times (c_1^{\text{F1/F2}}\sqrt{J+2} + c_2^{\text{F1/F2}}\sqrt{J})^2 + \frac{1}{2}(c_1^{\text{F1/F2}}\sqrt{J} - c_2^{\text{F1/F2}}\sqrt{J+2})^2, \quad (20)$$

and for the R3 and S1 branch ( $J' - J = +3/2$ )

$$I_{R3/S1(J)} = \frac{J+2}{2(2J+3)} \times (c_1^{\text{F1/F2}}\sqrt{J+1} - c_2^{\text{F1/F2}}\sqrt{J+3})^2. \quad (21)$$

## IV. ION DYNAMICS IN THE MULTIPOLE RF TRAP

In this section we establish the framework for a quantitative description of the dynamics of the trapped ions and finally describe the implementation of these elements in a Monte Carlo simulation of the dynamics of the trapped ions.

We thus consider an ensemble of ions trapped in the electrical potential of the RF trap defined by the geometry of the trap ( $r_0, L_0$ ), the end cap potentials ( $V_{\text{CE1-2}}$  and  $V_{\text{CX1-2}}$ ) and the amplitude  $V_{\text{RF}}$  and frequency  $f_{\text{RF}} = 4 \text{ MHz}$  of the radio frequency potential applied to the 16 pole electrodes; see Fig. 3 and Fig. 4. The ions interact with a thermalized He-buffer gas, among themselves, and with the ambient radiation field.

In the following subsections we describe a modeling of these interactions, then return to the ion motion in the trap potentials including space charge, and finally outline the Monte Carlo simulations applied to represent the ion dynamics in the trap and used to interpret the experimental observations.

### A. Collisions

The conditions for binary collisions among particles (either He-OH<sup>-</sup> or OH<sup>-</sup> - OH<sup>-</sup>) in thermal equilibrium are illustrated in Fig. 7(a) that shows the Maxwell-Boltzmann distributions of available collisional energies (energy in the center-of-mass  $E_{\text{cm}}$  of the collisional system) at various temperatures:

$$f(E_{\text{cm}})dE_{\text{cm}} = \frac{2}{\sqrt{\pi}} \sqrt{\frac{E_{\text{cm}}}{k_B T}} \frac{dE_{\text{cm}}}{k_B T} \exp\left(\frac{-E_{\text{cm}}}{k_B T}\right). \quad (22)$$

The energy thresholds for rotational excitations in OH<sup>-</sup> are also indicated to illustrate the possibilities for energy exchange between translational and rotational motion in dependence of temperature. Rotational deexcitation, i.e., rotational to translational energy transfer, is evidently allowed at all collisional energies, while a minimum energy is needed for the translation to rotational energy transfer.

#### 1. He-ion collisions

The ions interact with He atoms through binary collisions in a buffer gas at a density  $n_{\text{He}}$  and at a temperature  $T_{\text{He}}$ .

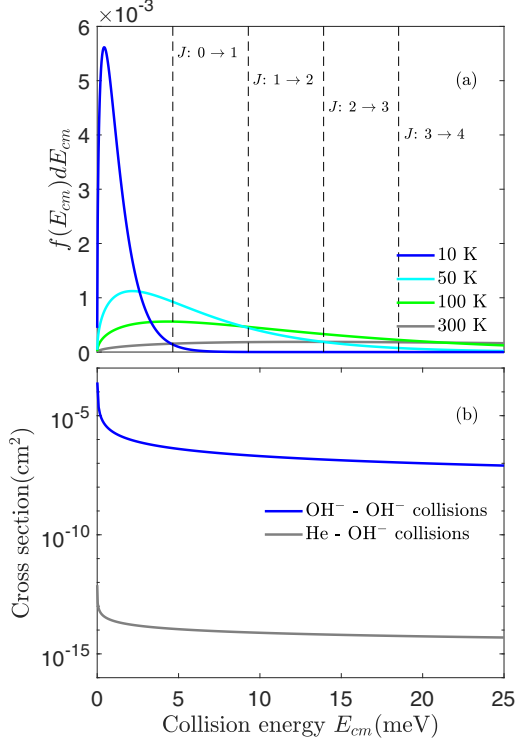


FIG. 7. (a) Maxwell-Boltzmann distributions of collisional energies at various temperatures following Eq. (22) and with  $dE_{cm} = 0.01$  meV. (b) Cross section for ion-ion [Eq. (27)] and He-ion collisions [Eq. (23)].

Thermalized He gas is constantly supplied to the trap, so the He-buffer gas can be seen as a heat reservoir that is unaffected by the trapped ions. The binary He-ion collisions can be either elastic, i.e., exchanging only kinetic energy and momentum, or inelastic, i.e., involving rotational excitation or deexcitation of the  $\text{OH}^-$  ions. Outside the ion-trap assembly, i.e., in the surrounding vacuum chamber, the gas temperature is  $T_{\text{CH}} \sim 300$  K and He atoms from this region can in principle propagate through the trap region and cause He-ion collisions at 300 K. An argument similar to the one provided in Sec. II C for estimating the He density inside the trap reveals, however, that the effect of warm He gas in the trap is most likely negligible, i.e., the density of cold He largely dominates.

Quantitatively, an ensemble of  $\text{OH}^-$  anions at a temperature  $T_i = 10$  K has a mean speed of  $v_{\text{OH}^-} = \sqrt{8/\pi} k_B T_i / m_{\text{OH}^-} = 112$  m/s, and hence a characteristic timescale for the ion motion in the trap is  $\sim 2 r_0 / v_{\text{OH}^-} = 90$   $\mu\text{s}$ .

The polarizability of He is  $\alpha_{\text{He}} = 0.208$   $\text{\AA}$  [66], and the corresponding Langevin cross section is (see, e.g., Ref. [44])

$$\sigma_L = \frac{q_i}{v_r} \sqrt{\frac{\pi \alpha_{\text{He}}}{\epsilon_0 \mu_{\text{He}}}} = \frac{q_i}{\sqrt{E_{cm}}} \sqrt{\frac{\pi \alpha_{\text{He}}}{2 \epsilon_0}}, \quad (23)$$

where  $v_r$  is the relative He-ion speed and  $\mu_{\text{He}} = 3.2$  amu is the reduced mass of the He- $\text{OH}^-$  collision system. The gray line in Fig. 7(b) shows the Langevin cross section as a function of collision energy for the He- $\text{OH}^-$  system. The corresponding Langevin rate coefficient for collisions under thermal equilib-

rium between the He gas and ion ensemble is

$$k_L = \int \sigma_L \sqrt{\frac{2E_{cm}}{\mu_{\text{He}}}} f(E_{cm}) dE_{cm} = q_i \sqrt{\frac{\pi \alpha_{\text{He}}}{\epsilon_0 \mu_{\text{He}}}}, \quad (24)$$

which evidently becomes temperature independent and is explicitly  $k_L = 5.9 \times 10^{-10}$   $\text{cm}^3 \text{s}^{-1}$ .

With a typical He pressure at 300 K of  $p_{\text{CH}}(300 \text{ K}) = 5 \times 10^{-6}$  mbar in our setup, the corresponding He density in the chamber is  $n_{\text{CH}}(300 \text{ K}) = p_{\text{He}} / k_B T_{\text{CH}} = 1.2 \times 10^{11} \text{ cm}^{-3}$ , and the corresponding He density inside the trap (at lower temperature  $T \sim 10$  K) is  $n_{\text{He}}(10 \text{ K}) = 4.3 \times 10^{12} \text{ cm}^{-3}$  as obtained from Eq. (4). Under these conditions, the typical timescale for He- $\text{OH}^-$  collisions is  $1/(n_{\text{He}} k_L) = 3.9 \times 10^2$   $\mu\text{s}$ . Thus, for the parameter regimes used in the present experiment, a trapped  $\text{OH}^-$  ion experiences typically  $\sim 0.23$  collisions with He atoms per round trip in the ion trap.

## 2. Ion-ion collision

The total effect of the trapped ion's mutual Coulomb interaction can be approximated by a space-charge potential (mean field approximation) that locally modifies the ions laboratory energies and hence effectively change the conditions for He-ion collisions and ion-ion collisions. We will describe this effect in Sec. IV C.

Neighboring ions (at the same local potential created by the trap fields and the space-charge potential) can collide in direct binary collisions and exchange energy and momentum as well as internal rotational energy. The volume of the region where ions are trapped can be roughly estimated as  $\sim L_0 \pi (r_0/2)^2 = 0.64 \text{ cm}^{-3}$ , where  $r_0/2$  represents an estimate of the radius of the ion ensemble. With a typical number of trapped ions  $N_i \sim 10^5$ , the ion density is  $n_i \sim 1.6 \times 10^5 \text{ cm}^{-3}$ . The typical distance between two ions can be estimated as  $d_i \sim (3/4\pi/n_i)^{1/3} \sim 115$   $\mu\text{m}$  and the corresponding potential energy is  $q_i^2/(4\pi\epsilon_0 d_i) \sim 13$   $\mu\text{eV}$ . The ratio (coupling parameter) of the interaction energy and the typical thermal energy scale ( $k_B T = 1.3$  meV at 10 K) can be evaluated as  $\Gamma = q_i^2/(4\pi\epsilon_0 d_i k_B T) = 1.5 \times 10^{-2}$ , showing that the ion motion in the trap is mostly governed by the confining potential.

Following Jackson [67], the Rutherford formula for the differential cross section for ion-ion scattering with an angular deflection  $\theta$  can be approximated as

$$\begin{aligned} \frac{d\sigma_C}{d\Omega} &= \left( \frac{q_i^2}{4\pi\epsilon_0} \right)^2 \frac{1}{16E_{cm}^2} \frac{1}{\sin^4(\theta/2)} \\ &\approx \left( \frac{q_i^2}{4\pi\epsilon_0} \right)^2 \frac{1}{E^2} \frac{1}{(\theta^2 + \theta_{\min}^2)^2} \end{aligned} \quad (25)$$

where the cutoff angle  $\theta_{\min}$  can be represented as the ratio of the de Broglie wavelength for the scattering systems and its dimension

$$\theta_{\min} = \frac{\hbar}{\sqrt{2\mu_i E_{cm}} r_{\text{OH}^-}}, \quad (26)$$

where  $\mu_i = 8.5$  amu is the reduced mass of the  $\text{OH}^- - \text{OH}^-$  system and where the internuclear distance of  $\text{OH}^-$  anions,  $r_{\text{OH}^-} = 9.7 \times 10^{-11}$  m, is used as a representative value for



the size of the scattering system. Under these conditions, the total cross section for Coulombic ion-ion collisions can be written as

$$\begin{aligned}\sigma_C &= \pi \left( \frac{q_i^2}{4\pi\epsilon_0} \right)^2 \frac{1}{E_{cm}^2} \frac{1}{\theta_{min}^2} \\ &= \pi \left( \frac{q_i^2}{4\pi\epsilon_0\hbar} \right)^2 \frac{2\mu_i r_{OH^-}^2}{E_{cm}} \\ &= \pi \left( \frac{q_i^2}{4\pi\epsilon_0\hbar} \right)^2 \frac{4r_{OH^-}^2}{v_r^2}.\end{aligned}\quad (27)$$

The total cross section for ion-ion collisions is displayed as the blue (black) line in Fig. 7(b). The temperature dependent (thermal equilibrium) rate coefficient [defined as in Eq. (24) using  $\sigma_C$  instead of  $\sigma_L$  and  $\mu_i$  instead of  $\mu_{He}$ ] for  $OH^- - OH^-$  collisions becomes for example  $k_C$  (10 K) =  $7.4 \times 10^{-3} \text{ cm}^3 \text{ s}^{-1}$  and  $k_C$  (300 K) =  $1.4 \times 10^{-3} \text{ cm}^3 \text{ s}^{-1}$ . The corresponding timescales for ion-ion collisions are  $1/[n_i k_C$  (10 K)]  $\sim 0.9$  ms and  $1/[n_i k_C$  (300 K)]  $\sim 5$  ms. Thus, ion-ion collisions at low temperature are approximately 5 times more frequent than at 300 K.

It should also be noted that binary ion-ion collisions of identical partners are more effective for exchange of energy and momentum than collisions between partners of unequal mass like the He- $OH^-$  collisions.

### 3. Inelastic collisions

In Fig. 7(a) the energy condition for collisional excitation of rotational levels of  $OH^-$  are indicated with vertical dashed lines that mark the threshold energies for transitions between neighboring rotational levels. To describe collision-induced rotational transitions we specify the cross section for both collisional excitation  $\sigma_{X,J}^{EX}$  and deexcitation  $\sigma_{X,J}^{dEX}$ , where the label  $X$  signifies either He-ion collisions ( $X = L$ ) or ion-ion collisions ( $X = C$ ).

To make a simple model, we assume that only transitions with a change of rotational quantum number  $\Delta J = \pm 1$  are possible for an  $OH^-$  irrespective of the collision partner (He or another  $OH^-$ ) and further that the total cross section for rotational transitions is proportional to the cross section for elastic collisions,

$$\sigma_{X,J}^{EX}(E_{cm}) + \sigma_{X,J}^{dEX}(E_{cm}) = a_X \sigma_X(E_{cm}), \quad (28)$$

with  $a_X < 1$ . The cross sections for either excitation and deexcitation are further made proportional to the degeneracy of the final state, hence for excitation

$$\sigma_{X,J}^{EX}(E_{cm}) \propto \begin{cases} (2J+3) & \text{for } E_{cm} \geq E_{J+1}^{OH^-} - E_J^{OH^-} \\ 0 & \text{otherwise} \end{cases} \quad (29)$$

and for deexcitation

$$\sigma_{X,J}^{dEX} \propto \begin{cases} (2J-1) & \text{for } J > 0 \\ 0 & \text{for } J = 0 \end{cases}. \quad (30)$$

### 4. Kinematics of elastic and inelastic collisions

To describe explicitly the effect of binary collisions on the motion of the trapped ions, we consider an ion at position  $x$ ,

$y, z$  and with velocities  $v_{i,x}, v_{i,y}, v_{i,z}$  that experience a collision with another particle at the same location and with velocities  $v_{p,x}, v_{p,y}, v_{p,z}$ , where  $p$  represents a He atom or another ion.

The center of mass (cm) velocities for the collision system is

$$v_{cm,\alpha} = \frac{m_p \times v_{p,\alpha} + m_i \times v_{i,\alpha}}{m_p + m_i} \quad (31)$$

and the relative speed of the collision is computed as

$$v_r = \sqrt{\sum_{\alpha} (v_{p,\alpha} - v_{i,\alpha})^2}, \quad (32)$$

with a corresponding relative energy  $E_{cm} = 1/2 \mu v_r^2$ , where  $\mu = m_p m_i / (m_p + m_i)$ .

The velocities of the  $OH^-$  ion in the center of mass system is obtained as

$$v_{cm,i,\alpha} = v_{i,\alpha} - v_{cm,\alpha}, \quad (33)$$

and the corresponding speed in the cm systems before the collision is

$$v_{cm,i} = \sqrt{\sum_{\alpha} (v_{cm,i,\alpha})^2} = \frac{\mu}{m_i} \times v_r. \quad (34)$$

From energy and momentum conservation, the velocities of the  $OH^-$  ion in the in cm frame after the collision are

$$u_{cm,i,\alpha} = -v_{cm,i,\alpha}. \quad (35)$$

Finally, the velocities of the ion in the laboratory frame after the collision are

$$u_{i,\alpha} = u_{cm,i,\alpha} + v_{cm,\alpha}. \quad (36)$$

If the collision is inelastic, i.e., an energy  $\Delta E$  is released (rotational deexcitation) or absorbed (rotational excitation) in the collision, the relative velocity in the  $cm$  frame is corrected to

$$v_r^* = \sqrt{\frac{2(E_r - \Delta E)}{\mu}} \quad (37)$$

and the velocities after the collision to

$$u_{cm,i,\alpha} = -v_{cm,i,\alpha} \times \frac{v_r^*}{v_r}. \quad (38)$$

### B. The ambient radiation field

The ion trap assembly is kept at temperature  $T_{cryo}$  via the cryo-cooler and the trapped ions are exposed to the radiation field at this temperature. The openings at the exit and entrance side of the trap also allow radiation from the ambient 300 K radiation field to penetrate into the trap. These thermal radiation fields at temperature  $T$  can be characterized by their energy density (Planck distribution)

$$\rho(\omega, T) d\omega = \frac{\hbar\omega^3}{\pi^2 c^3} \times \frac{d\omega}{\exp(\hbar\omega/k_B T) - 1}, \quad (39)$$

where the photon energy is given by  $E_\gamma = \hbar\omega$ . An estimate of the amount of the 300 K radiation that enters into the trap region can be obtained by considering the open solid angle of the trap region towards the outside. The opening angle is

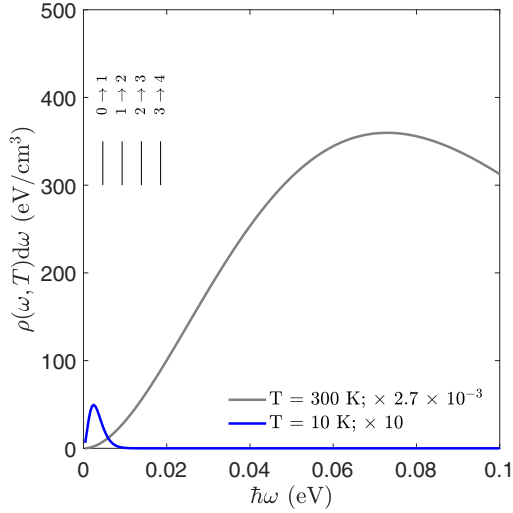


FIG. 8. Spectral energy density of thermal radiation at 300 K and 10 K plotted with  $d\omega = 6.28 \times 10^{11} \text{ s}^{-1}$ . The 300 K field is scaled with the factor  $2.7 \times 10^{-3}$  that represents an estimate of the fraction of this field that enters the region of the RF trap assembly where  $\text{OH}^-$  ions are trapped. The 10 K field is scaled by a factor of 10 to be visible on the chosen linear scale. The vertical solid lines and annotations in the upper left corner illustrate the energy location of the first rotational transitions in  $\text{OH}^-$  as calculated using Eq. (8).

approximately  $\theta_t \sim \tan^{-1}(3/40) = 4.2^\circ$  and the fraction of the total solid angle (including both entrance and exit sides) is therefore  $\sim [1 - \cos(\theta_t)] = 2.7 \times 10^{-3}$ . To illustrate quantitatively the possible effect of these radiation fields on the trapped  $\text{OH}^-$  ions, Fig. 8 shows the spectral densities for both 300 K and 10 K thermal radiation fields scaled to be comparable on a linear scale. Evidently, despite the limiting solid angle, the 300 K thermal radiation completely dominates the thermal radiation inside the trap. The relevant rotational transitions of  $\text{OH}^-$  are found on the low energy side of the 300 K radiation field where indeed the spectral density is nonvanishing.

The corresponding emission and absorption rates for rotational transitions for  $\text{OH}^-$  have been determined experimentally [31] and computationally [52] and found to be small. Thus, Meyer *et al.* [31] reported experimental values for the lifetimes (inverse of Einstein A coefficients) for the lowest the rotational states  $J = 1-3$  to be  $\sim 193 \text{ s}$ ,  $\sim 20.9 \text{ s}$ , and  $\sim 5.30 \text{ s}$ , respectively, i.e., providing a timescale for the radiative coupling much longer than the estimated He-ion and ion-ion collisional timescales ( $\sim \text{ms}$ ).

### C. Trapped ion motion with He-buffer gas

The trapping of an individual ion of mass  $m_i$  and charge  $q_i$  in the RF trap is governed by the effective potential energy (here neglecting the dependence on the azimuthal angle) [35]

$$U_{\text{eff}}(r) = \frac{1}{8} \frac{(q_i V_{\text{RF}})^2}{\epsilon_c} \left( \frac{r}{r_0} \right)^{2n-2}, \quad (40)$$

where  $n = 8$  for our 16-pole trap and  $r_0 = 5 \text{ mm}$ , and where the characteristic energy  $\epsilon_c$  is given by

$$\epsilon_c = \frac{m_i (2\pi f_{\text{RF}})^2 r_0^2}{2n^2}, \quad (41)$$

so  $\epsilon_c = 21.7 \text{ eV}$  for  $\text{OH}^-$  in the present situation with  $f_{\text{RF}} = 4 \text{ MHz}$ . The effective potential is simply given by  $V_{\text{eff}} = U_{\text{eff}}/q_i$ . The possible radial extent of the motion of a (stably) trapped ion, i.e., where its motion is adiabatic with respect to the radio-frequency field, is classified by the adiabaticity parameter

$$\eta = \frac{n-1}{n} \frac{q_i V_{\text{RF}}}{\epsilon_c} \left( \frac{r}{r_0} \right)^{n-2} \quad (42)$$

in the sense that stable trapping is obtained for  $\eta \lesssim \eta_{\text{max}} = 0.3$  [35,43,68]. The maximum radius of stable ion trapping can then be expressed as

$$r_{\text{max}} = r_0 \left( \eta_{\text{max}} \frac{n}{n-1} \frac{\epsilon_c}{q_i V_{\text{RF}}} \right)^{1/(n-2)}. \quad (43)$$

To illustrate the properties of the effective potential, the dashed black line in Fig. 9(a) shows  $V_{\text{eff}}(r)$  for  $\text{OH}^-$  with  $V_{\text{RF}} = 30 \text{ V}$ . The maximum radius [Eq. (43)] allowing adiabatic motion is shown as a vertical dashed line.

For an ensemble of *noninteracting* ions with potential energies  $U_{\text{eff}}(r)$  [Eq. (40)] and in equilibrium with a heat reservoir at temperature  $T$  (canonical ensemble), the ion density (i.e., the phase-space density after integrating over the particle momenta) can be written as

$$n_i(r) = \frac{N_i}{\delta V_i} \times \exp\left(\frac{-U_{\text{eff}}(r)}{k_B T}\right), \quad (44)$$

where  $N_i$  is the total number of ions and  $\delta V_i$  is the effective volume occupied by the ions given explicitly by

$$\begin{aligned} \delta V_i &= \int_0^{r_{\text{max}}} \int_0^{2\pi} \int_0^{L_0} r \, dr \, d\theta \, dz \\ &= 2\pi L_0 \int_0^{r_{\text{max}}} \exp\left(\frac{-U_{\text{eff}}(r)}{k_B T}\right) r \, dr. \end{aligned} \quad (45)$$

Here perfect cylindrical symmetry is assumed and the effect of end cap potentials is neglected. In Ref. [68] we gave a more elaborate outline of the basic statistical description of an ion ensemble in an RF trap.

When more ions are trapped in the RF trap, a first approximation of the effect on the motion of an individual ion can be obtained by considering the mean field of all ions, i.e., effectively the space-charge potential that results from the ion density  $n_i(r)$ . To evaluate the space-charge potential explicitly, we first evaluate the electric field from a cylindrically symmetric ion density distribution

$$\mathbf{E}_{\text{sp}}(r) = \mathbf{e}_r \frac{q_i}{\epsilon_0} \frac{1}{r} \int_0^r n_i(r) r \, dr. \quad (46)$$

If we define the electric potential to be zero at the location of the RF-electrodes, i.e., at the radius  $r = r_0$ , the resulting space-charge potential can be calculated as

$$V_{\text{sp}}(r) = - \int_{r_0}^r \mathbf{E}_{\text{sp}}(r) \cdot d\mathbf{r}. \quad (47)$$

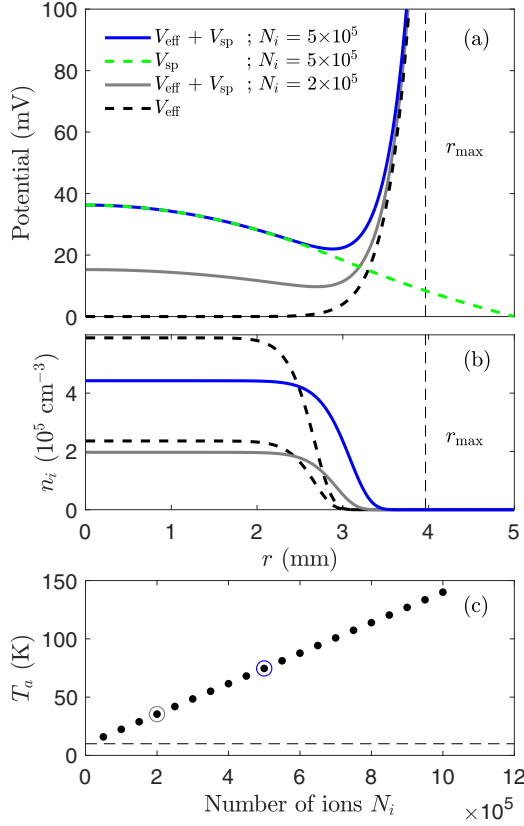


FIG. 9. Illustration of potentials, ion densities, and effective He-ion collision temperature in the RF trap. (a) Radial potential for  $\text{OH}^-$  in the RF trap for  $V_{\text{RF}} = 30$  V. The dashed black line shows the effective potential ( $V_{\text{eff}} = U_{\text{eff}}/q_i$ ) from Eq. (40) for  $V_{\text{RF}} = 30$  V. The dashed vertical line marked  $r_{\text{max}}$  indicates the maximum radius [Eq. (43)] below which the ion motion can safely be considered adiabatic. The full blue (black) and gray lines show total potentials including contributions from the space charge of all ions for  $N_i = 5 \times 10^5$  and  $N_i = 2 \times 10^5$ , respectively. The green (gray) dashed line indicates the contribution from space charge for  $N_i = 5 \times 10^5$ . (b) Radial density of trapped ions. The dashed lines show the ion distributions without the space charge for  $N_i = 5 \times 10^5$  and  $N_i = 2 \times 10^5$ , and the blue (black) and gray lines show the corresponding distributions including the space charge. (c) The apparent ion temperature as calculated from Eq. (53). Note that this temperature is not a measure of the temperature of the He-ion collisions. The blue (black) and gray circles indicate the apparent temperatures for the potentials and densities given with blue (black) and gray lines in panel (a)–(b).

The total potential seen by an individual ion in the trap can then be written

$$V_{\text{tot}}(r) = V_{\text{eff}}(r) + V_{\text{sp}}(r). \quad (48)$$

In general, Eq. (46) and Eq. (47) are most easily solved numerically, but for reference, simple analytical solutions can be obtained for a uniform ion distribution:

$$n_i(r) = \begin{cases} n_0 & \text{for } r \leq r_i \\ 0 & \text{for } r > r_i \end{cases}. \quad (49)$$

In this special case, Eqs. (46) and (47) result in an electric field of

$$\mathbf{E}_{\text{sp}}(r) = \mathbf{e}_r \frac{q_i n_0}{2\epsilon_0} \begin{cases} r & \text{for } r \leq r_i \\ \frac{r_i^2}{r} & \text{for } r > r_i \end{cases} \quad (50)$$

and a space-charge potential of

$$V_{\text{sp}}(r) = \frac{q_i n_0}{2\epsilon_0} \begin{cases} r_i^2 \ln\left(\frac{r_i}{r_0}\right) + \frac{1}{2}(r^2 - r_i^2) & \text{for } r \leq r_i \\ r_i^2 \ln\left(\frac{r}{r_0}\right) & \text{for } r > r_i \end{cases}. \quad (51)$$

Evidently, as depicted in Eq. (48), the space potential will affect the total potential of an ion relative to the pure electric potential ( $V_{\text{eff}} = U_{\text{eff}}/q_i$ ) imposed by the trap electrodes and hence, the ion density will adapt dynamically to the combination of trap potentials and space charge. The actual resulting space-charge potential and radial ion distribution can be approximated by an iterative procedure where first a zero-order ion density  $n_i^0$  is obtained from Eq. (44) with  $T^0 = T_{\text{He}}$ . Then, the corresponding space-charge field ( $\mathbf{E}_{\text{sp}}^0$ ) and space-charge potential ( $V_{\text{sp}}^0$ ) are obtained by numerical integration of Eqs. (46) and (47) which together gives a zero-order total potential  $V_{\text{tot}}^0(r) = V_{\text{eff}}(r) + V_{\text{sp}}^0(r)$ . From this total potential, a mean kinetic energy of the ion ensemble as induced by the potentials can be estimated as

$$E_k^0 = \frac{\int q_i [V_{\text{tot}}^0(r) - V_{\text{tot}}^0(0)] n_i^0(r) r dr}{\int n_i^0(r) r dr}. \quad (52)$$

Thereafter, a first-order apparent ion temperature can be estimated as

$$T_a^1 = T_{\text{He}} + \frac{2E_k^0}{3k_B}. \quad (53)$$

This first-order temperature ( $T_a^1$ ) is then applied in Eq. (44) to yield a first-order ion density  $n_i^1(r)$  and another iteration is done. With this method, self-consistent values of ion density  $n_i(r)$ , space-charge potential [ $V_{\text{sp}}(r)$ ], and apparent ion temperature ( $T_a$ ) are obtained within a few iterations. We note that our iterative approach is fundamentally different from the one described in Ref. [44] as we consistently use  $U_{\text{eff}}(r)$  in Eq. (44) and explicitly not  $q_i V_{\text{tot}}^j$ , where  $j$  numbers the iteration step.

The method described here is evidently approximate as the apparent temperature  $T_a$  does not correspond to a Maxwell-Boltzmann distribution of He-ion velocities at this temperature. Instead, the resulting distribution of He-ion collisional velocities will be narrow, i.e., with a Maxwell-Boltzmann velocity distribution corresponding to the laboratory temperature of He (approximately 10 K) but offset with the speed at each location in the trap.

Figures 9(a) and 9(b) show examples of the resulting total potentials and radial ion distributions for noninteracting ions (black dashed lines) and for interacting ions with two different total numbers of ions (blue (black) and gray lines) and Fig. 9(c) shows the computed apparent temperature [Eq. (53)] as a function of the number of ions.

The additional available kinetic energy of the ions in the presence of space charge relative to the He-buffer gas is clearly evident as the total potential develops a minimum at

larger radii [see Fig. 9(a)], and the depth of the minimum increases with the number of ions ( $N_i$ ). Fig. 9(b) illustrates the radial widening of ion distributions in the presence of space charge. However, it should be explicitly noted that despite the widening due to space charge, all ions in the ensemble are still very well within the adiabatic region of the trap.

It should be noted that the effect of space charge on ion-ion collisions will also be significant although two colliding ions are also at the same space-charge potential, since the relative velocity and hence the collision energy depends on the direction of motions of the two colliding ions.

A consequence of the space charge for the collisional dynamics in the trap, both considering He-ion and ion collisions, is for example that the concept of thermal equilibrium (e.g. the concept of rate coefficients [Eq. (24)] for the description of collisions evidently fails, since the He-ion and ion-ion velocities are forced to vary strongly in dependence of the position inside the trap.

#### D. Model of ion motion and cooling

Based on the descriptions in the previous sections, we here describe the implementation of a numerical model that we use to gain insight into the cooling of trapped ions. The model includes the propagation of a selected number of ions  $N_{is}$  ( $\sim 500$ ) for a certain time  $t_{is}$  ( $\sim 25$  ms) with a fixed time-step  $dt$  ( $1 \mu s$ ) during trapping in the RF trap potential and further subject to collisions with He gas with a temperature  $T_{He}$  and with a density  $n_{He}$  as well as to collisions with trapped ions with a density  $n_i$ .

In the model, the motion of an individual ion is described classically in the adiabatic potential of the RF trap, i.e., according to the equation of motion

$$\frac{d\mathbf{p}_i}{dt} = -\nabla V_{\text{eff}}(r), \quad (54)$$

where  $\mathbf{p}_i$  is the momentum of the ion. If the space charge from all other trapped ions should be taken into account, the motion of an independent ion, could more correctly be described with  $V_{\text{tot}}(r)$  [Eq. (48)] in place of  $V_{\text{eff}}(r)$  in Eq. (54). However, when the independent particle description is invalid, for instance by imposing He-ion or ion-ion collisions, a description with  $V_{\text{tot}}$  in Eq. (54) no longer applies; for example the ion density would unrealistically re-adapt to the space-charge potential. Clearly, if the number of ions included in the simulation is sufficiently large, i.e., equal to the actual number of trapped ions, all ion-ion interactions could be directly included in Eq. (54). However, this introduces significant computational overhead and complexity and hence we settle on the approximate description of individual ions given by Eq. (54) and include the consequences of the space-charge potential in the implementation of collisions as described next.

Collisions are implemented as random events with a Monte Carlo simulation. Thus, for each ion and for each time step of the simulation, it is decided if a collision should take place based on collision probabilities  $P_{He}$  for He-ion collisions and  $P_i$  for ion-ion collisions that we describe in detail below. In case both types of processes are selected for a given time step, it is again randomly decided which one should actually occur. For example, a collision with a He atom is selected to occur

in a given time step based on a random number  $h_1$  drawn between 0 and 1, i.e., a collision will take place if  $P_{He} \leq h_1$ . It is then similarly decided if the collision should be elastic or inelastic based on another random number  $h_2$  between 0 and 1 that is compared to the chosen value of  $a_L$  [Eq. (28)] (or  $a_C$  in case of a selected ion-ion collision). Last, if the collision is inelastic, it is randomly decided if the collision should be an excitation or a deexcitation based on the assumed cross section ratios for these processes given by Eq. (29) and Eq. (30).

To include the effect of space charge in the simulation, we note that the local modification of an ion's speed due to the space-charge potential at the radial location  $r$  is given by

$$\Delta v_{i,\text{sp}}(r) = \sqrt{\frac{2E_i(r) + 2q_i[V_{\text{sp}}(r) - V_{\text{sp}}(0)]}{m_i}} - \sqrt{\frac{2E_i(r)}{m_i}}, \quad (55)$$

where  $E_i(r)$  is the laboratory kinetic energy of the ion when moving in the effective potential [ $V_{\text{eff}}(r)$ ] only. The consequence of this extra velocity is taken into account in two ways. First, to account for the space-charge effect on the direct ion motion, i.e., the effect that the ion in fact move faster than anticipated directly from solving Eq. (54), we introduce an extra positional step in the numerical integration, so the spatial position of an ion is displaced by  $\Delta v_{i,\text{sp}} \times dt$  in the direction of motion obtained directly from Eq. (54). Second, the extra ion velocity due to space charge, Eq. (55), is taken into account in the evaluation of collision probabilities ( $P_{He}$  and  $P_i$ ) and in the kinematics of the actual collisions.

For an ion to experience a collision with a He atom, the collision probability in a time interval  $dt$  is

$$P_{He} = 1 - \exp\left(-dt \times n_{He} \times \int v_r \sigma_{He}(v_r) g_{He}(v_r, x, r) dv_r\right) \quad (56)$$

where  $\sigma_{He}$  is the collision cross section and  $g_{He}(v_r, x, r)$  represents the distribution of relative He-ion speeds ( $v_r$ ) at the location ( $x, r$ ) inside the trap, which is in general not uniform as illustrated with the evaluation of the space-charge potential in Sec. IV C. If the collision cross section is assumed to be the Langevin cross section i.e.,  $\sigma_{He} = \sigma_L$  [Eq. (23)], the proportionality  $\sigma_L \propto 1/v_r$ , makes the collision probability for He-ion collisions constant, so  $P_{He} = 1 - \exp(-k_L n_{He} dt)$ . To allow for a deviation of the He-ion cross section from the strict  $1/v_r$  dependence and include the space-charge-induced velocity, we adapt the following collisional probability

$$P_{He} = 1 - \exp[-v_{i,He} \sigma_{He}(v_{i,He}) n_{He} dt], \quad (57)$$

where  $v_{i,He} = \langle v_i \rangle + \Delta v_{i,\text{sp}}(r)$  and  $\langle v_i \rangle$  is the ensemble average of the ion speed.

To simulate an actual He-ion collisions, provided it has been selected from the collision probability in a given time step, a He atom with velocities randomly drawn from Maxwell-Boltzmann distributions [Eq. (1)] at a temperature  $T_{He} = T_{\text{cryo}}$  is selected. To include the effect of space charge, the extra speed is added as  $\pm 1/3 \Delta v_{i,\text{sp}}$  to each velocity component of the selected He atom, where the sign is the same as the sign for the original He atom's velocity component. This He atom is then collided with the ion as outlined in Sec. IV A 4 giving new velocities to the ion after the collision.

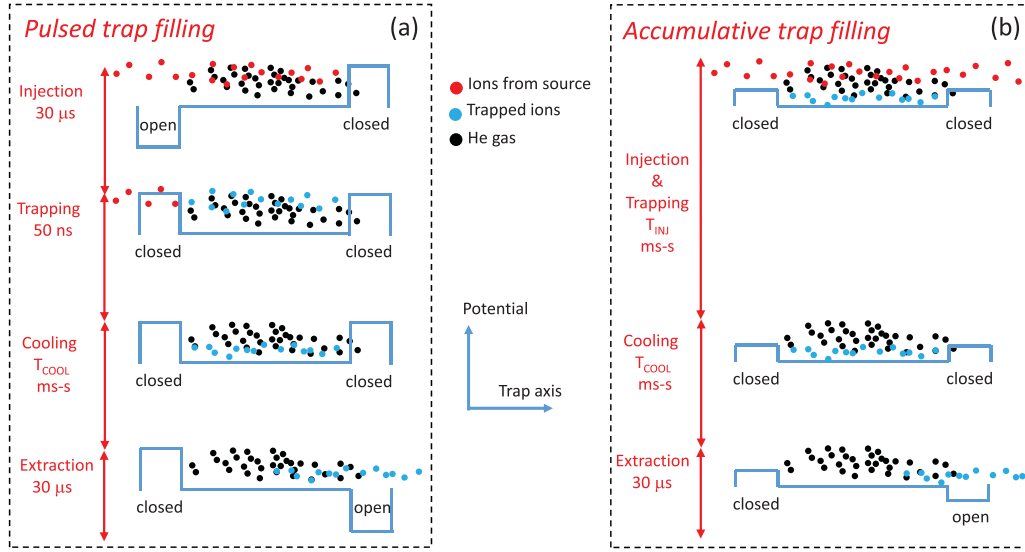


FIG. 10. Illustration of trap operation with pulsed trap filling and accumulative trap filling.

For ion-ion collisions, the collision probability is similar to Eq. (56) given by

$$P_i = 1 - \exp\left(-dt \times \int v_r \sigma_C(v_r) g_i(v_r, x, r) n_i(r) dv_r\right). \quad (58)$$

Contrary to the case for He-ion collisions, the collision probability for ion-ion collisions will certainly have an explicit dependence on the distribution of relative speeds (collision energies) since the cross section for Coulomb collisions is not proportional to  $1/v_r$ . Again, the distribution  $g_i(v_r, x, r)$  of ions with relative speed  $v_r$  with respect to the chosen ion would in principle be available from many particle simulations, but in practice, we decide to make a more approximate formulation. We thus choose to define an average ion-ion collision speed as  $v_{i,C} = 1/2[\langle v_i \rangle + \Delta v_{i,sp}(r)]$ , as representative of the local condition inside the trap and hence we simplify Eq. (58) to

$$P_i = 1 - \exp[-v_{i,C} \sigma_C(v_{i,C}) n_i dt]. \quad (59)$$

Finally, to simulate an actual ion-ion collision for a selected ion, the velocities of a collision partner is randomly drawn from Maxwell-Boltzmann velocity distributions of temperature

$$T_{i,sp} = \frac{2}{3k_B} \langle E_i \rangle, \quad (60)$$

and the velocity of this collision partner is adjusted with  $+1/3(\Delta v_{i,sp}/2)$  in each direction to account for the effect of local space charge. Note that this velocity correction is not dependent on sign as was the case for He-ion collisions since the ionic collision partner itself is subject to the space charge. This is also the reason for the division by two in the velocity offset as compared to the case for He-ion collisions. The ion-ion collision kinematics for the ion in collision with this partner is evaluated as described in Sec. IV A 4.

## V. RESULTS

### A. Operation of the RF trap

Figure 10 illustrates schematically two different methods of operation of the RF trap with ion filling from a decelerated ion beam. In the first method, labeled pulsed trap filling, the trap loading proceeds by first lowering the potentials on the entrance cap electrodes ( $V_{CE1}$  and  $V_{CE2}$ ) to leave the entrance side open while the potentials on the cap electrodes on the exit side ( $V_{CX1}$  and  $V_{CX2}$ ) are set high to close this side of the trap. Using the chopper (Fig. 1), an ion pulse is released from the ion source, enters the trap volume, and is reflected from the exit side. While the ion pulse still fills the trap, the entrance caps are switched to high levels thereby closing the trap. After loading, the ions are kept trapped for a time  $T_{COOL}$  (see also Fig. 2) and then extracted by lowering the potentials on the cap electrodes on the exit side ( $V_{CX1}$  and  $V_{CX2}$ ).

In the second method of operating, labeled accumulative trap filling, the trap loading proceeds by realizing a long pulse from the source and keeping the trap cap electrodes statically on for a time  $T_{INJ} + T_{COOL}$  at potentials that allow a fraction of ions from the ion beam to enter the trap volume (and in principle even pass directly through the trap) but still leave an axial potential well inside the trap volume that can confine ions of even lower energy. During residence in the trap, some incoming ions will collide with He atoms or already trapped ions and thereby loose energy and eventually be trapped. The ion cooling and extraction proceeds as described for the first method of operation.

With the first method (pulsed ion filling), the trap filling can be completed fast ( $\sim \mu s$ ) and does not depend significantly on the applied He gas density. However, the final achievable ion density in the trap is determined by the intensity of the incoming beam and the potentials on the entrance and exit electrodes are bound to higher values that ensures blockage of all ions from the incoming beam.

With the second method (accumulative ion filling), the momentary trap filling is less efficient and strongly dependent on the density of cold particles in the trap (He gas and already

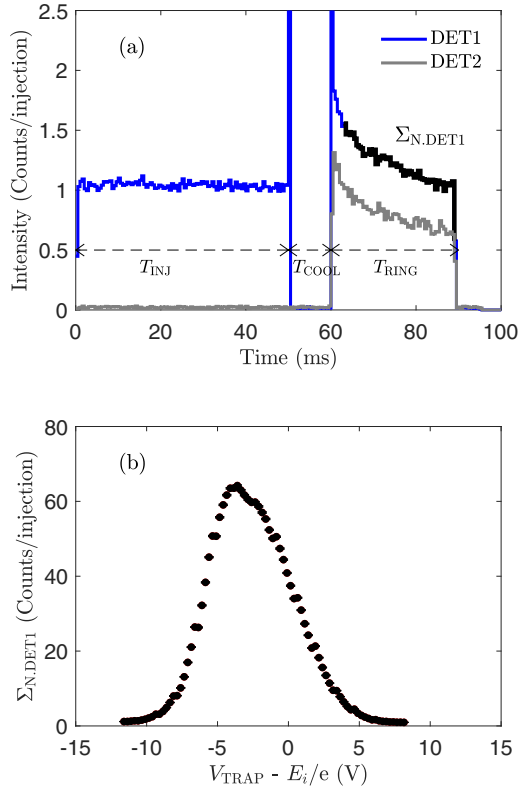


FIG. 11. (a) Observation of particles on DET1 and DET2 as a function of time during the experimental cycle of injection, trapping, and storage (see Fig. 1) for trap potential  $V_{\text{TRAP}}$ ,  $E_i/e = -3.7$  V, under cold conditions  $T_{\text{cryo}} \sim 6$  K, and operated with accumulative filling of the trap [Fig. 10(b)]. The section of the signal from DET1 marked with a black (bold) coloring is the region which is summed to yield the integrated intensity  $\Sigma_{\text{N,DET1}}$ . (b) Integrated intensity ( $\Sigma_{\text{N,DET1}}$ ) during storage in the SAPHIRA as a function of the of the RF trap potential  $V_{\text{TRAP}}$  (see Fig. 3) as referred to the equivalent ion potential.

trapped ions). This method, however, benefits from the possibility to inject over extended times whereby an adjustable (and for example high) ion density can be achieved even for an initially weak ion beam, and, moreover, the cap potentials can be kept low. All data presented in this paper are obtained with the accumulative mode of ion filling.

To characterize the trap operation with respect to trapping dynamics and efficiency, we use an experimental scheme where  $T_{\text{COOL}} = 10$  ms and  $T_{\text{RING}} = 30$  ms are fixed while  $T_{\text{INJ}}$ , the trap temperature (6 K or 300 K) as well as the trap potential ( $V_{\text{TRAP}}$ ), and the He density ( $n_{\text{He}}$ ) are varied. We note that the cooling time in the trap is kept relatively short for these investigations, since a complete thermalization of translational or internal motions is not important for demonstrating the basic trap operation.

Figure 11(a) shows an example of measured count rates on DET1 and DET2 (see Fig. 1) as a function of time during this operation. The significant intensity observed with DET1 during the injection period ( $T_{\text{INJ}}$ ), stems from ions leaking through the RF trap, proceeding into the SAPHIRA storage ring, making one round-trip, and finally exiting the ring towards DET1, since the potentials on the first corner

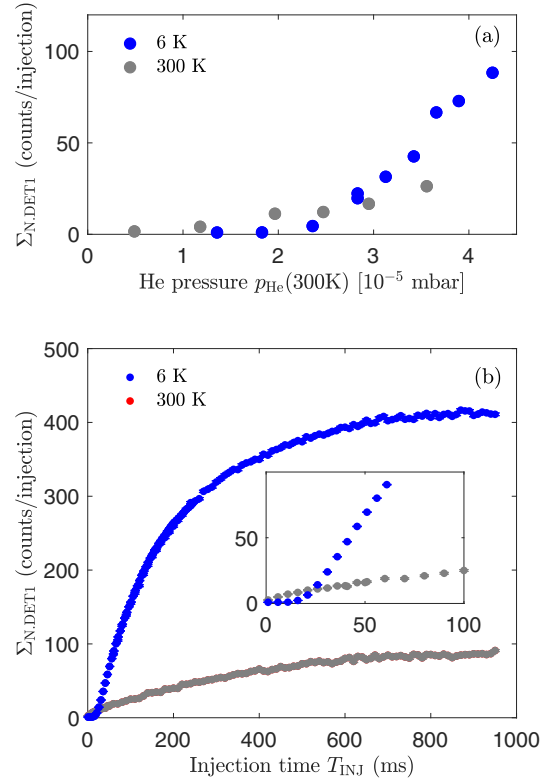


FIG. 12. Illustration of the operation of the RF trap accumulative trap filling [see Fig. 10(b)]. (a) Integrated intensity [ $\Sigma_{\text{N,DET1}}$ , see Fig. 11(a)] during storage in the SAPHIRA as a function of the measured He pressure in the vacuum chamber at 300 K. The timing settings were  $T_{\text{INJ}} = 50$  ms,  $T_{\text{COOL}} = 10$  ms, and  $T_{\text{RING}} = 30$  ms. (b) Integrated intensity during storage in the SAPHIRA with a measured He pressure of  $p_{\text{CH}} = 3.8 \times 10^{-5}$  mbar as a function of the applied injection time  $T_{\text{INJ}}$  and with  $T_{\text{COOL}} = 10$  ms and  $T_{\text{RING}} = 30$  ms.

of SAPHIRA are off during this period. During the cooling time, the ion injection is halted, i.e., the chopper has a high potential and the ion pulse is off (see Fig. 1 and Fig. 2) and only few random counts are observed on DET1. During the period  $T_{\text{RING}}$ ,  $\text{OH}^-$  ions are circulating in SAPHIRA (round trip time of  $\sim 18 \mu\text{s}$ ) and the signals observed on DET1 and DET2 during this time originates from products of neutralization of  $\text{OH}^-$  during storage. From measurements with longer storage times, the lifetime of the  $\text{OH}^-$  beam in SAPHIRA was determined to be  $(155 \pm 2)$  ms for a ring pressure of  $8 \times 10^{-9}$  mbar.

Figure 11(b) shows the integral number of counts  $\Sigma_{\text{N,DET1}}$  as a function of the trap potential  $V_{\text{TRAP}}$ . This number is a representative measure for the amount of ions in the RF trap. As seen, under the conditions of accumulative filling, the most efficient filling of the trap is obtained with a potential  $V_{\text{TRAP}}$  a few volts lower than the equivalent ion potential  $E_i/e$ . It should be noted that the SAPHIRA storage ring has a relatively wide energy acceptance of a few percent of the total energy (4 keV), so we do not expect any major effects of intensity loss due to a mismatch the trap potential and the SAPHIRA ring setting for small changes of the energy of the extracted ions. Figure 12 shows the intensity of trapped ions

as a function of the measured He pressure [Fig. 12(a)] and the period of injection [Fig. 12(b)] for the RF trap operated at room temperature and under cryogenic conditions. Similar to the data in Fig. 11, the intensity of trapped ions is quantified from the integrated intensity ( $\Sigma_{N,DET1}$ ) of neutralized particles during ion storage in SAPHIRA being proportional to the number of ions injected from the ion trap.

For the investigated pressure change in the RF trap of  $0.5\text{--}4.5 \times 10^{-5}$  mbar, the corresponding change of the pressure in SAPHIRA was  $\sim 0.1 \times 10^{-9}$  mbar giving a possible 10% variation of the summed intensity, which is insignificant for the systematic trends seen in Fig. 12(a). At room temperature (300 K), the summed intensity increases essentially linearly with the applied He pressure, while a clear nonlinear rise is observed for cold conditions. This provides an experimental evidence that the ensemble of already trapped ions in the ion trap plays a significant role for the further trapping of ions when the trap is cold, i.e., the importance of ion-ion collision becomes comparable to the importance of He-ion collisions for trapping at cryogenic temperatures.

This is further demonstrated in Fig. 12(b) that displays the summed intensity as a function of injection time and for an approximately constant He density  $n_{He} = 3.3 \times 10^{12} \text{ cm}^{-3}$  (with  $p_{CH} = 3.8 \times 10^{-5}$  mbar). For a trap temperature of 300 K, the summed intensity rises almost linearly for low injection times and shows signs of saturation at longer times. For the case of 6 K, again a clear nonlinear rise of the summed intensity is seen. Moreover, the trapping intensity is generally stronger compared to the 300 K case, but it also displays signs of saturation at long injection times.

Summarizing, it is clear that accumulative trap filling of the trap is the attractive scheme at low temperature and for beams of low intensity, since the final ion-beam intensity in SAPHIRA can be well controlled by simple variation of the injection time  $T_{INJ}$ . Additionally, the effect of ion-ion collision for the trapping efficiency, i.e., essentially elastic ion-ion collisions between trapped and translationally cold ions and new incoming ions, is very significant for the trapping.

## B. Rotational cooling of $\text{OH}^-$

### 1. Photodetachment of stored $\text{OH}^-$ in SAPHIRA

Figure 13 displays an example of the directly observed intensity on DET2 as a function of time obtained with conditions for observing photodetachment of  $\text{OH}^-$  during storage in SAPHIRA. The laser-induced photodetachment intensity is clearly identified as a sharp peak in red (bold), and with a summed intensity  $\Sigma_{L,DET2}$ . The corresponding intensity without photons  $\Sigma_{LB,DET2}$  is estimated from summing the intensity in the time interval exactly one revolution in SAPHIRA before the laser firing time. In Fig. 13 the summed intensities  $\Sigma_{B,DET2}$  and  $\Sigma_{N,DET2}$  are also indicated which represent estimates of the background noise on the DET2 and the intensity of trapped ions, respectively.

Under stable conditions of the ion-photon overlap in SAPHIRA, the photodetachment cross section of  $\text{OH}^-$  at a given photon energy  $E_\gamma$  can then be evaluated as

$$\sigma_D(E_\gamma) \propto \frac{\Sigma_{L,DET2}(E_\gamma) - \Sigma_{LB,DET2}}{(N_\gamma(E_\gamma))(\Sigma_{N,DET2} - \Sigma_{B,DET2})}, \quad (61)$$

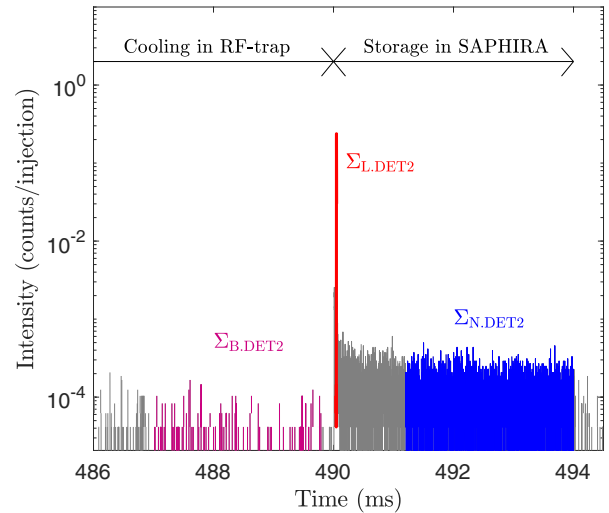


FIG. 13. Photodetachment of  $\text{OH}^-$  after injection and trapping in the RF trap for  $T_{INJ} + T_{COOL} = 490$  ms, followed by storage in SAPHIRA for  $T_{INJ} = 4$  ms. Laser pulses are merged with the ion beam after  $T_L = 40 \mu\text{s}$  of storage giving rise to the sharp signal marked in red (bold). The purple (gray) curve marks the measured counts ( $\Sigma_{B,DET2}$ ) that are used to represent the background noise counts on DET2. Similarly, the blue (black) curve marks the counts ( $\Sigma_{N,DET2}$ ) that is used to determine the intensity of stored ions.

where  $\langle N_\gamma(E_\gamma) \rangle$  is the average number of photons (pulse energy/photon energy) in a laser pulse.

The experiment was run in a stable mode with almost no variation of the number of ions during scanning of the photon energy, and in practice the normalization to the number of ions, i.e., the factor  $(\Sigma_{N,DET2} - \Sigma_{B,DET2})$  in the denominator of Eq. (61) is of no practical importance.

To quantify the number of ions in the RF trap based on the measurement from the stored beam in SAPHIRA we define the quantity

$$\eta_{\text{OH}^-} = \frac{\Sigma_{N,DET2} - \Sigma_{B,DET2}}{P_{\text{RING}}} \quad (62)$$

that provides an estimate of the ion intensity corrected for the variation of residual gas density in the SAPHIRA ring due to different He pressures in the RF trap.

Figure 14 shows three examples of measurements of the relative  $\text{OH}^-$  photodetachment cross section near threshold obtained at different temperatures of the RF trap assembly as well as different He pressures and amount of ion loading. Each spectrum is fitted with the photodetachment model given in Eq. (7) with the amplitude factor  $\sigma_0$ , the rotational temperature  $T_R$ , and the background cross section spectra  $\sigma_B$  as free parameters.

The origin of the measured background cross section originates from a small fraction of  $^{17}\text{O}^-$  from the ion source also occurring at mass  $\sim 17$  amu. This was confirmed by observing the onset of a weak signal from threshold photodetachment of  $\text{O}^-$  the region  $E_\gamma = 1.44\text{--}1.49$  eV. Further, by mass selecting  $^{16}\text{O}^-$  directly from the ion source, injecting and cooling these ions in the RF trap, followed by transfer to SAPHIRA, and performing photodetachment in the region  $E_\gamma = 1.79\text{--}1.85$  eV it was confirmed that the signal from  $\text{O}^-$  detachment is

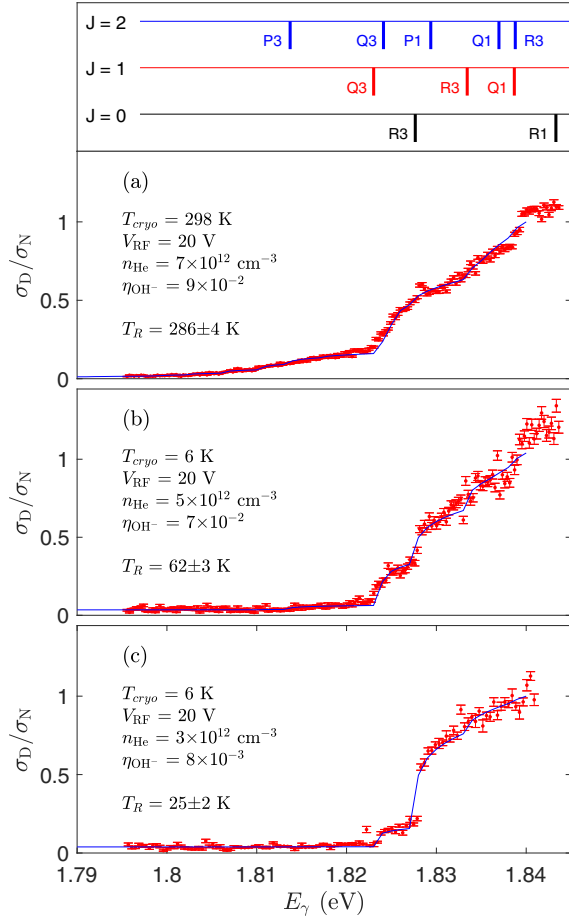


FIG. 14. Photodetachment cross sections for  $\text{OH}^-$  near threshold as measured with a trapped, extracted, and stored beam in SAPHIRA (see Fig. 1) obtained under different operational conditions of the RF trap system as indicated in the individual panels (a)–(c). The measured cross sections are normalized to the cross section  $\sigma_N$  obtained at  $E_\gamma = 1.84$  eV.

essentially constant in this energy range. The value of the exponent  $p_\beta$  in Eq. (6) was initially adjusted when fitting the coldest spectra [the example in Fig. 14(c)] where only few transitions are contributing to the signal. The best representation of the spectra is observed with  $p_\beta = 0.2$ , and this value is then used in all fits, i.e., also neglecting a possible variation on the actual transition  $\beta$ . The fit to the coldest spectra [Fig. 14(c)] also allows us to quantify the contribution from  $^{17}\text{O}^-$  and we find  $\sigma_B/\sigma_N = (3.9 \pm 0.1) \times 10^{-2}$ .

The fits of the spectra with Eq. (7) displays a small variation with the exact energy calibration of the laser which we know to an accuracy of approximately  $\pm 0.3$  nm. To accommodate this uncertainty, we increase the reported uncertainty on the fits by 1 K beyond the error determined directly from the fit.

## 2. Rotational temperature of $\text{OH}^-$ in the RF trap

Figure 15 shows the fitted rotational temperatures obtained as exemplified in Fig. 14 under adjusted conditions of temperature, RF-amplitude, He density, and the number of trapped

ions. As mentioned, in practice, the number of trapped ions is varied by changing the injecting time  $T_{\text{INJ}}$ .

Under warm conditions, i.e., at  $T_{\text{cryo}} = 300$  K [red (black) star and red (black) open circles in Fig. 15] the rotational temperature of  $\text{OH}^-$  is found as  $T_R \sim T_{\text{cryo}}$  possibly with a weak increase as a function of the number of ions.

Under cold condition of the cryo-cooler (i.e., at  $T_{\text{cryo}} = 6$  K), the fitted rotational temperatures of  $\text{OH}^-$  displays systematically almost linear dependencies on the number of ions in the trap when the other variables of the system ( $V_{\text{RF}}$ ,  $n_{\text{He}}$ ) are held constant.

From the data displayed in Fig. 15 it is moreover clear that the most important parameters that control the rotational temperature are indeed the number of ions ( $n_{\text{He}}$ ) and the He density ( $n_{\text{He}}$ ). For example, with  $V_{\text{RF}} = 30$  V and  $n_{\text{He}} = 50 \times 10^{12} \text{ cm}^{-3}$  (higher He density, green (gray) dots in Fig. 15), the rotational temperature increases steeply as a function of the number of stored ions. When lowering the He density to  $n_{\text{He}} = 10 \times 10^{12} \text{ cm}^{-3}$ , (light gray dots in Fig. 15), the rotational temperature still increases as a function of the number of ions but with a slope smaller by a factor of  $\sim 16$ .

In comparison, the variation with the RF-amplitude ( $V_{\text{RF}}$ ) shows (at most) a minor impact on the rotational temperatures as can be seen by comparison of the purple ( $V_{\text{RF}} = 10$  V) and green points ( $V_{\text{RF}} = 30$  V) obtained with comparable He densities where variations of the rotational temperature with the number of ions are very similar. The RF amplitude essentially controls the radial extent of the ion ensemble inside the RF trap [Eq. (43)] and hence the proximity of the trapped ions to the rods with the time-varying RF field.

All data displayed in Fig. 15 for cold conditions of the trap, point towards two central conclusions from the experimental observations, namely, that rotationally cold  $\text{OH}^-$  can be obtained with a low number of ions in the RF trap and with a low He density. Under the conditions realized here it also appears that the He density in fact sets the lower limit to which rotational temperature can be reached in the limit of low ion densities. Thus, at higher He densities  $\sim 50 \times 10^{12} \text{ cm}^{-3}$ , the limit of rotational temperature seems to be  $T_R \sim 50$ – $60$  K while at lower He densities  $\sim 5 \times 10^{12} \text{ cm}^{-3}$  rotational temperatures  $T_R \sim 20$ – $25$  K are reached with the present experimental system.

Figure 16 displays the measured rotational temperature of  $\text{OH}^-$  as a function of storage time in SAPHIRA, i.e., after which time the photodetaching laser is fired. It can be seen that the rotational temperature remains almost constant during the first 50 ms, possibly with a weak rising tendency as indicated with the dashed black line.

## 3. Interpretation of cooling dynamics

The observation that the rotationally coldest ions can be obtained with the lowest number of ions in the trap points to the importance of ion-ion interactions for the thermalization of the trapped ions. As described in Sec. IV C, the effect of space charge (mean ion-ion interaction) evidently complicates the translational and rotational collision dynamics for an ensemble of trapped ions as the space-charge potential imposes regions of the trap with elevated He-ion and ion-ion collision energies (see also Sec IV D). The observed tendency



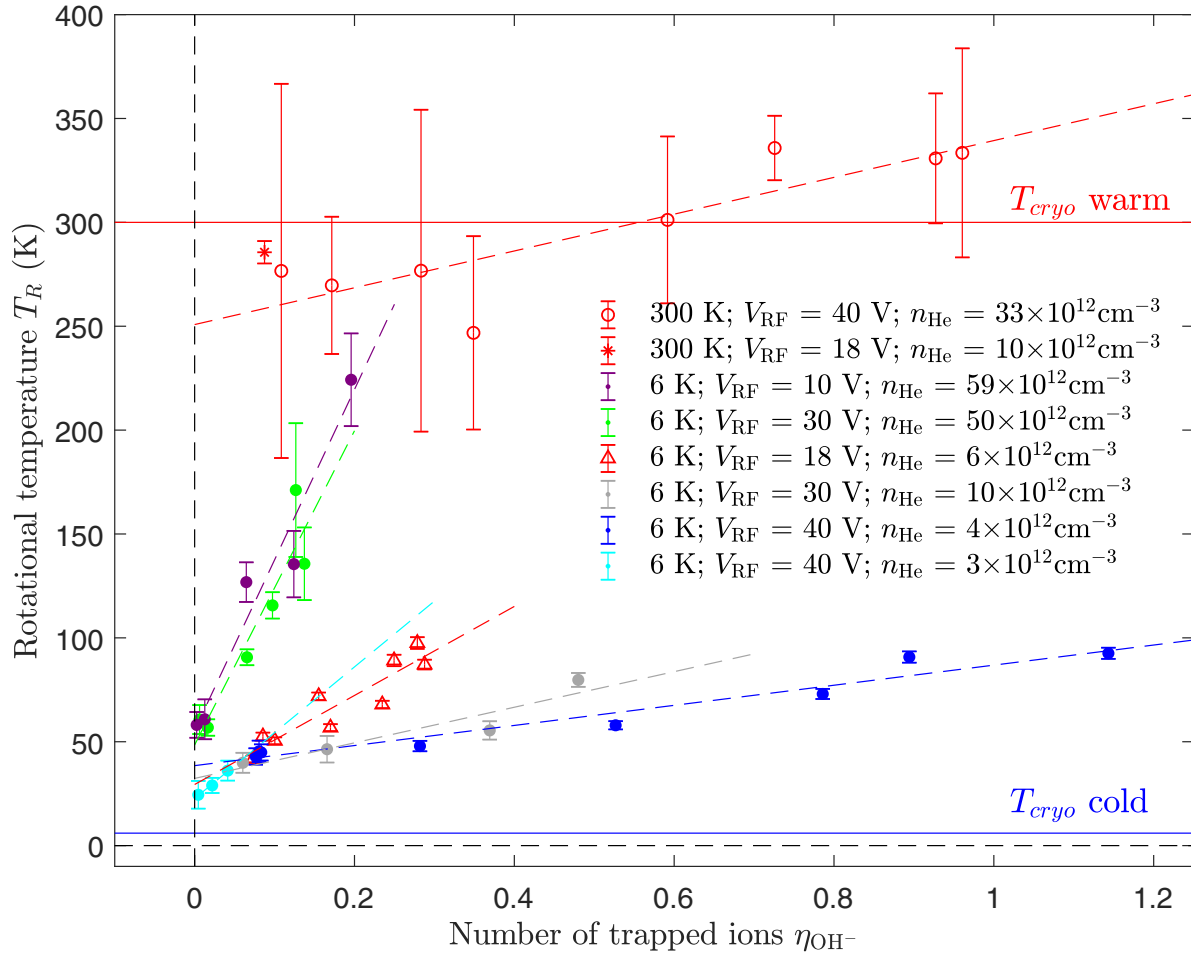


FIG. 15. Rotational temperature of  $\text{OH}^-$  as a function the number of trapped ions represented by the parameter  $\eta_{\text{OH}^-}$  [see Eq. (62)] for varying conditions of the RF trapping, i.e., the temperature of the cryo-cooler, RF amplitude  $V_{\text{RF}}$ , and He density  $n_{\text{He}}$  inside the RF trap assembly.

that fewer ions lead to a colder rotational temperature seems intuitively clear since the effect of space charge to locally increase collision energies is smaller for fewer ions in the trap. The effects of space charge can of course be made totally

negligible by lowering the number of ions towards one, but in practice a significant number of ions are needed for carrying out experiments with the cooled ions.

The observation that a low He density is also a criterion for obtaining rotationally cold  $\text{OH}^-$  ions is perhaps less intuitive as one might expect more He to provide a stronger coupling [several collisions per round trip in the trap (90  $\mu\text{s}$ )] between the trapped ion ensemble and hence provide a more efficient cooling. As illustrated in Fig. 15, the experimental evidence contradicts this and instead indicates that a weak coupling ( $< 1$  collision per round trip in the trap) between the trapped ions and the He gas is favorable. This observation can for example be rationalized if the validity of the  $1/v_r$  dependency of the Langevin cross section is not taken as representative for He-ion collisions, such that the He-ion collision probability becomes dependent on the relative velocity and hence on the ion location in the trap. Assuming still that the He-ion cross section is maximal at low energy, with a weak coupling to the He gas, the probability of He-ion collisions will be favored in regions of low collision velocity and hence allow a thermalization temperature closer to the He temperature. Oppositely, with a strong coupling between the He gas and the ion ensemble, corresponding to several He-ion collisions per round trip in the trap, the full space-charge-induced velocity

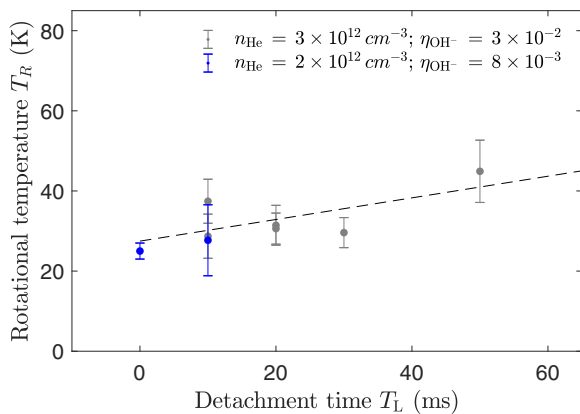


FIG. 16. Rotational temperature of  $\text{OH}^-$  as a function storage time in SAPHIRA obtained with  $T_{\text{cryo}} = 6 \text{ K}$ ,  $V_{\text{RF}} = 40 \text{ V}$ , and He density ( $n_{\text{He}}$ ) in the RF trap and number of ions ( $\eta_{\text{OH}^-}$ ) as indicated in the legend. The shown data is obtained with  $p_{\text{RING}} = 8.1 \times 10^{-9} \text{ mbar}$ .

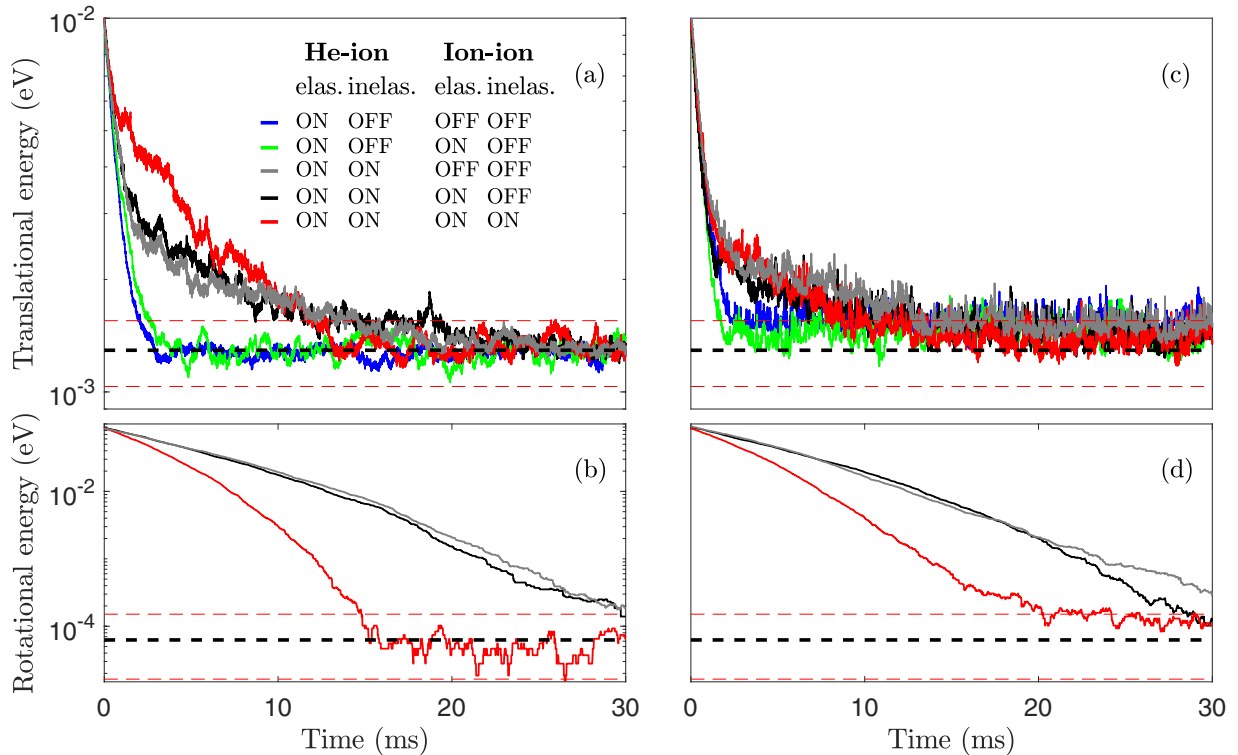


FIG. 17. Results of numerical simulations of  $\text{OH}^-$  ion motion and collisions in a RF trap with He-buffer gas at temperature  $T_{\text{He}} = 10$  K and density  $n_{\text{He}} = 4 \times 10^{12} \text{ cm}^{-3}$ . The ion density was set to  $n_i = 5 \times 10^5 \text{ cm}^{-3}$ , corresponding to approximately  $N_i = 2.5 \times 10^5$ . Five different types of simulations are shown with different aspects of the collisional dynamics (He-ion and ion-ion collisions, either purely elastic or also inelastic) activated as defined in panel (a). For each type of simulation, a total of  $N_{\text{is}} = 5 \times 10^3$  ions are propagated with time step of  $dt = 1 \mu\text{s}$  and a simulation is run (a)–(b) without inclusion of space charge ( $V_{\text{sp}} = 0$ ), and (c)–(d) with inclusion of space charge. The horizontal dashed lines in each panel, shows the mean energy corresponding to He temperature 10 K (black) as well as 8 K (lower red) and 12 K (upper red).

spread will be forced to be explored and thus fundamentally limit the reachable rotational temperature in excess of the He temperature.

The observation that the He density is also decisive for the rotational temperature of  $\text{OH}^-$  reached when the ion density is low, i.e., the different limiting values when  $\eta_{\text{OH}^-} \sim 0$  seen in Fig. 15, can, in our view, have two different origins. First, the ion micro-motion in the time-dependent RF field where the ions turn around in the trap [35] will in general lead to locally elevated collision energies. Hence, if collisional heating in the RF field is important, the same argument of a necessity of a low He density (weak He-ion coupling) to obtain the coldest ions apply, since the weak coupling will in general emphasize the regions of low collision speed where the collision cross section is the highest. Second, the extraction and acceleration of the  $\text{OH}^-$  out of the trap to achieve the transfer of ions to the SAPHIRA storage ring will expose the  $\text{OH}^-$  ions to a large variation of collision energies that can also lead to rotational heating [29]. A high He density will also favor heating by this mechanism and again the low He density will be a criterion for obtaining the coldest ions. In the particular case of  $\text{OH}^-$ , the extraction and acceleration is accomplished in  $\sim 10 \mu\text{s}$ . The number of He collisions experienced by an extracted  $\text{OH}^-$  can be roughly estimated as  $10 \mu\text{s}/n_{\text{He}}k_L$  (see Sec. IV A 1) which yields  $\sim 0.03$  collisions for  $n_{\text{He}} = 5 \times 10^{12} \text{ cm}^{-3}$  and  $\sim 0.3$  collisions for  $n_{\text{He}} = 5(\times 10^{12} \text{ cm}^{-3})$ . Thermalization of the ion ensemble to the He buffer gas temperature requires  $\sim 10$

collisions per ion (see the following Sec. V C), i.e., an average ion will experience  $\sim 1/300$  or  $\sim 1/30$  of the necessary collisions for complete thermalization during extraction. Thus, a variation collisional heating during the ion extraction from the RF trap as function of the He buffer gas density cannot be neglected under the conditions of the present experiments, and the observed variation of rotational temperatures in the limit of low ion number ( $\eta_{\text{OH}^-} \sim 0$ ) seems very likely to be attributed to the effect of such collisions. It should be pointed out that the effect of collisional heating during ion extraction is sensitive to the particular ion under study through variations of both the reaction rate coefficient ( $k_L$ ) and the extraction time.

### C. Modeling of ion cooling

To illustrate the dynamics of the cooling, both neglecting and including space charge, we made simulations as described Sec. IV D. For each simulation, ions are randomly distributed in the volume of the trap and given a uniform distribution of translational energy with a mean of 10 meV (maximum energy 20 meV). The ions are similarly given a rotational excitation corresponding to a uniform distribution of rotational levels with  $J = 0$ –10.

Figures 17(a) and 17(b) display results of a series of simulations (see Sec. IV D) on an ensemble of  $N_{\text{is}} = 500$  trapped  $\text{OH}^-$  ions where the effect of space charge is neglected

( $\Delta v_{i,sp} = 0$ ). The conditions of the simulations are further detailed in the figure caption. As indicated in the figure, results from simulations are shown where both elastic and inelastic collisions are included (ON) or neglected (OFF).

The blue and green curves in Fig. 17(a) illustrate equilibration of the translational ion motion when only elastic collisions are included. Under the defined conditions of temperature and He density, the ion ensemble is seen to stabilize at a mean energy of to 1.2 meV (10 K) in  $\sim 3$  ms which corresponds to  $\sim 0.25$  collisions per round trip in the trap with  $n_{\text{He}} = 4 \times 10^{12} \text{ cm}^{-3}$ . An average of 8-9 collisions for each  $\text{OH}^-$  ion is found to be required to achieve the thermalization. Under conditions of only elastic collisions, the cooling of the ion ensemble proceeds in the same way irrespective of the inclusion of the ion-ion collisions (blue and green curves are very similar) despite the fact that the ion-ion collision frequency is comparable to that of the He-ion collisions. This is expected as the ion-ion collisions evidently are not able to couple energy out of the ensemble of trapped ions.

Including rotational transitions as a fraction ( $a_L = 0.2$ ) of the He-ion collisions as defined in Eq. (28), and with a branching of excitation and deexcitation given by Eqs. (29) and (30), leads to a slower translational cooling [ $\geq 25$  ms for the present conditions, gray and black curves in Fig. 17(a)] and a cooling of the rotational motion of the  $\text{OH}^-$  ions towards the He temperature on a longer timescale. This illustrates the significant role of elastic ion-ion collisions to redistribute the released energy from the rotational motion into translation motion among the trapped ions.

Including also inelastic ion-ion collisions [ $a_C = 0.2$ , red curves in Figs. 17(a) and 17(b)], both translational and rotational cooling is realized faster, both in approximately 20 ms. This again identifies the ion-ion collisions as important for the redistribution of energy inside the ion ensemble. Here in particular, ion rotational energy is efficiently transferred to the ion translational energy through ion-ion collisions from where it is removed (cooled) by He-ion collisions.

In Figs. 17(c) and 17(d) the result of simulations are shown where the effect of space charge is included as described in Sec. IV D. When only elastic collisions are included (blue and green lines) the cooling takes places on about the same timescale as when space charge is neglected [Fig. 17(a)], but a temperature ( $\sim 12$  K) higher than the temperature of the He gas is reached. This is intuitive as the presence of space charge imposes some collisions at higher energy.

When including inelastic collisions, the same general trends are observed for the cooling of the translational motion as without space charge, but the initial cooling phase ( $\sim 0-7$  ms) appears more effective and the effect of inelastic ion-ion collisions is less pronounced. The thermal equilibrium is reached at approximately the same time (15–20 ms). However, including space charge, the rotational thermalization is seen to be slowed down with respect to the situation without space charge. This is in fact rational as the elevated collision energies due to space charge favors rotational excitation as illustrated in Fig. 7(a). Hence under the influence of space charge, translational energy will be coupled more likely to rotational energy and the total process of rotational cooling will take longer.

## VI. DISCUSSION

### A. Rotational cooling of $\text{OH}^-$

In previous studies on rotational state cooling of ions trapped in an RF trap [48–52], it was observed that the final reachable rotational temperature generally exceeds the temperature of the trap assembly. Explanations for this effects have been perused in [51] in terms of radio-frequency heating (He-ion collisions in the time-dependent field), influence of geometrical distortions of the trap electrode, rotational excitation by blackbody radiation from outside the trap, or incomplete thermalization of the buffer gas to the cryo-cooler, but no conclusive understanding has been obtained.

In this study, we also observe rotational temperatures  $T_R$  in excess of the temperature  $T_{\text{cryo}}$  of the trap assembly. The systematic studies of the rotational temperature of  $\text{OH}^-$  obtained at different operating conditions of the trap presented in Fig. 15 indicate that the origin of the derivation between the gas temperature and the rotational temperature of the ions should be found in the combination of the space charge from trapped ions that locally increases the He-ion collision energy and the strength of the coupling between the He-buffer gas and the trapped ions. Thus, perhaps counter intuitive, the coupling to the He gas should be weak (low He density) to obtain the most effective cooling, since the trapped ions will tend to collide with He in regions of low collision energy. With a strong coupling of the trapped ions to the He gas, i.e., with many collisions per round trip in the trap, the ions must adapt to the complete energy variation of the He-ion collision energies throughout the trap. The strong dependency of the obtained rotational temperature on the He gas density emphasizes the approximate nature of the Langevin representation of the cross section for He- $\text{OH}^-$  collisions.

We speculate that the offset of the rotational temperature from the temperature of the trap seen in previous experiments [48–52] could indeed be related to the application of a high He density; for example, in Refs. [51,52], a He density of  $\sim 10^{14} \text{ cm}^{-3}$  was applied. In this connection, we again wish to stress that additional rotational heating due to He-ion collisions in regions of the trap where the ion micromotion [35] is significant or due to He-ion collision during the period of extraction and acceleration from the trap are suppressed at low He density. Hence, in all cases, the criterion of low He density to obtain the coldest ions seems important. The experimental evidence presented in Fig. 15 seems to indicate that the influence of the RF-amplitude is negligible for the rotational temperature possibly suggesting that the effect of He-ion collisions in the time-dependent fields is small.

Our numerical studies demonstrate the role of ion-ion collisions, i.e., among particles of equal mass, as an effective way of redistributing the translational and rotational energy among the trapped ions. Thus, the Coulomb repulsion can mediate a faster cooling of the internal energy by conversion of internal energy to translational energy that is then cooled by collisions with buffer gas. This effect may be of even higher significance in future studies on larger molecules, where the favorable sharing of energy among collision partners of equal mass is even more pronounced than for the present situation with He- $\text{OH}^-$  and  $\text{OH}^- - \text{OH}^-$  ion collisions.

From the numerical simulations, it is also a clear observation that the apparent ion temperature ( $T_a$ ) as derived from the calculations of the space-charge potential and the iteratively determined ion density in the trap [Fig. 9(c)] is not representative for the actual translational nor rotational temperature of the ions, but rather a parameter that solely enables a description of the ion density distribution. The reason for this is that the collisional conditions imposed by the space charge is not represented by thermal (Maxwell-Boltzmann) velocity distributions and that the collision cross sections strongly depends on velocity, so collisions (assuming a low number of collision per round trip, i.e., weak coupling) will be preferred in certain parts of the trap.

The numerical model, we have used to illustrate the ion dynamics in the RF trap (Sec. IV D) is evidently approximate in nature as it neglects the micro-motion of the ions in the RF field and uses classical simplified representations of the cross sections for He-ion and ion-ion collisions, and it does not account for the full dynamical problem in the trap, but rely on Monte Carlo simulations where average rate coefficients are used to evaluate collisional probabilities.

It would in principle be possible to assume certain He-ion elastic and inelastic cross sections and attempt to reproduce the observed dependencies of the rotational temperatures of  $\text{OH}^-$  on the He density to explicitly demonstrate that rotational cooling is achieved with a weak He-ion coupling. However, we refrain from this type of simulation as we cannot predict nor have sufficient knowledge on the actual cross sections for this to be meaningful. Instead, we wish to emphasize that theoretical efforts to clarify in more detail the He-ion and ion-ion elastic and inelastic scattering cross sections would be very valuable as would full many-particle simulations including interactions on an individual ion level.

Finally, as a possible improvement of the cooling capabilities of our present system, in future experiments we wish to explore the possibility of adding other gasses beyond He to the system as was recently proved effective for obtaining cold anions of ozone [69].

## VII. CONCLUSION

In this paper we have described the realization of a cryogenically cooled multipole radio-frequency trap and

demonstrated cooling of  $\text{OH}^-$  ions to  $\sim 25$  K as probed by threshold photodetachment of ions extracted from the trap. The RF trap is setup inline between the ion source plus mass separation and the molecular physics experimental system (storage ring, lasers, and detectors) where the cold ions are to be investigated (see Fig. 1).

The feasibility of the inline geometry relies on the development of efficient injection and extraction from the RF trap at high potential as also establish in previous studies [18,41,68,70]. An important advantage of the inline configuration is that it allows universal cooling of ions independent of ion source and that the accumulation and cooling can be done on one particular ion species. This indeed opens several exciting scientific opportunities. For example, intense beams of several negative ions can be produced from sputter ion sources, but the molecular ion beams are typically vibrationally and rotationally very hot [71]. With the system, we can cool these hot ions prior to the experiment and hence obtain a better initial state preparation of importance for example to understand cooling mechanism of molecules [71–75]. Also for complex or bio-molecular systems [29,37,76], that are typically produced by electrospray ionization, the possibility to accumulate and cool mass selected species to cryogenic temperatures may lead to feasible experiments even with very low DC currents from the ion source.

Finally, through interpretation of the experimental results and partly supported by numerical simulations, we believe an understanding of the limiting factors for rotational cooling of  $\text{OH}^-$  in RF traps is emerging. Thus, the coldest ensemble of ions can be obtained in with a weak coupling to He-buffer gas and a weak space-charge potential which in practical terms means a low He density and as low as number of ions as experimentally feasible.

## ACKNOWLEDGMENTS

We wish to thank the staff at the electrical and mechanical workshop at the Department of Physic and Astronomy at Aarhus University for excellent support during the design and setup of the RF trap system.

- 
- [1] D. Zajfman, O. Heber, L. Vejby-Christensen, I. Ben-Itzhak, M. Rappaport, R. Fishman, and M. Dahan, Electrostatic bottle for long-time storage of fast ion beams, *Phys. Rev. A* **55**, R1577 (1997).
  - [2] H. T. Schmidt, H. Cederquist, J. Jensen, and A. Fardi, Conetrap: A compact electrostatic ion trap, *Nucl. Instrum. Methods Phys. Res. B* **173**, 523 (2001).
  - [3] O. Aviv, Y. Toker, M. Errit, K. G. Bhushan, H. B. Pedersen, M. L. Rappaport, O. Heber, D. Schwalm, and D. Zajfman, A bent electrostatic ion beam trap for simultaneous measurements of fragmentation and ionization of cluster ions, *Rev. Sci. Instrum.* **79**, 083110 (2008).
  - [4] M. Lange, M. Froese, S. Menk, J. Varju, R. Bastert, K. Blaum, J. R. Crespo López-Urrutia, F. Fellenberger, M. Grieser, R. von Hahn, O. Heber, K.-U. Kühnel, F. Laux, D. A. Orlov, M. L. Rappaport, R. Repnow, C. D. Schröter, D. Schwalm, A. Shornikov, T. Sieber, Y. Toker *et al.*, A cryogenic electrostatic trap for long-time storage of keV ion beams, *Rev. Sci. Instrum.* **81**, 055105 (2010).
  - [5] J. B. Greenwood, O. Kelly, C. R. Calvert, M. J. Duffy, R. B. King, L. Belshaw, L. Graham, J. D. Alexander, I. D. Williams, W. A. Bryan, I. C. E. Turcu, C. M. Cacho, and E. Springate, A comb-sampling method for enhanced mass analysis in linear electrostatic ion traps, *Rev. Sci. Instrum.* **82**, 043103 (2011).

- [6] C. J. Johnson, B. B. Shen, B. L. J. Poad, and R. E. Continetti, Photoelectron-photofragment coincidence spectroscopy in a cryogenically cooled linear electrostatic ion beam trap, *Rev. Sci. Instrum.* **82**, 105105 (2011).
- [7] L. S. Harbo, S. Dziarzhyski, C. Domesle, G. Brenner, A. Wolf, and H. B. Pedersen, Lifetime of low vibrational levels of the metastable  $\tilde{B}^2B_2$  state of  $\text{H}_2\text{O}^+$  probed by photodissociation at 532 nm, *Phys. Rev. A* **89**, 052520 (2014).
- [8] S. Knauer, P. Fischer, G. Marx, M. Müller, M. Rosenbusch, B. Schabinger, L. Schweikhard, and R. N. Wolf, A multi-reflection time-of-flight setup for the improvement and development of new methods and the study of atomic clusters, *Int. J. Mass Spectrom.* **446**, 116189 (2019).
- [9] S. P. Møller, Elisa, and electrostatic storage ring for atomic physics, *Nucl. Instrum. Methods Phys. Res. A* **394**, 281 (1997).
- [10] T. Tanabe, K. Chida, K. Noda, and I. Watanabe, An electrostatic storage ring for atomic and molecular science, *Nucl. Instrum. Methods Phys. Res. A* **482**, 595 (2002).
- [11] S. Jinno, T. Takao, Y. Omata, A. Satou, H. Tanuma, T. Azuma, H. Shiromaru, K. Okuno, N. Kobayashi, and I. Watanabe, TMU electrostatic ion storage ring designed for operation at liquid nitrogen temperature, *Nucl. Instrum. Methods Phys. Res. A* **532**, 477 (2004).
- [12] J. Bernard, G. Montagne, R. Brédy, B. Terpend-Ordaciere, A. Bourgey, M. Kerleroux, L. Chen, H. T. Schmidt, H. Cederquist, and S. Martin, A tabletop electrostatic ion storage ring: Mini-ring, *Rev. Sci. Instrum.* **79**, 075109 (2008).
- [13] K. E. Stiebing, V. Alexandrov, R. Dörner, S. Enz, N. Yu. Kazarinov, T. Kruppi, A. Schempp, H. S. Böcking, M. Völp, P. Ziel, M. Dworak, and W. Dilfer, FLSR—The Frankfurt low energy storage ring, *Nucl. Instrum. Methods Phys. Res. A* **614**, 10 (2010).
- [14] H. T. Schmidt, R. D. Thomas, M. Gatchell, S. Rosén, P. Reinhed, P. Löfgren, L. Brännholm, M. Blom, M. Björkhage, E. Bäckström, J. D. Alexander, S. Leontein, D. Hanstorp, H. Zettergren, L. Liljeby, A. Källberg, A. Simonsson, F. Hellberg, S. Mannervik, M. Larsson *et al.* First storage of ion beams in the double electrostatic ion-ring experiment: DESIREE, *Rev. Sci. Instrum.* **84**, 055115 (2013).
- [15] H. B. Pedersen, A. Svendsen, L. S. Harbo, H. V. Kiefer, H. Kjeldsen, L. Lammich, Y. Toker, and L. H. Andersen, Characterization of a new electrostatic storage ring for photofragmentation experiments, *Rev. Sci. Instrum.* **86**, 063107 (2015).
- [16] M. O. A. El Ghazaly, ELASR—An electrostatic storage ring for atomic and molecular physics at KACST, *Results Phys.* **5**, 60 (2015).
- [17] R. von Hahn, A. Becker, F. Berg, K. Blaum, C. Breitenfeldt, H. Fadil, F. Fellenberger, M. Froese, S. George, J. Göck, M. Grieser, F. Grussie, E. A. Guerin, O. Heber, P. Herwig, J. Karthein, C. Krantz, H. Kreckel, M. Lange, F. Laux, A. P. O. Connor, and S. Sunil Kumar, The cryogenic storage ring CSR, *Rev. Sci. Instrum.* **87**, 063115 (2016).
- [18] Y. Nakano, Y. Enomoto, T. Masunaga, S. Menk, P. Bertier, and T. Azuma, Design and commissioning of the RIKEN cryogenic electrostatic ring (RICE), *Rev. Sci. Instrum.* **88**, 033110 (2017).
- [19] U. V. Pedersen, M. Hyde, S. P. Møller, and T. Andersen, Lifetime measurement of  $\text{He}^-$  utilizing an electrostatic ion storage ring, *Phys. Rev. A* **64**, 012503 (2001).
- [20] P. Reinhed, A. Orbán, J. Werner, S. Rosén, R. D. Thomas, I. Kashperka, H. A. B. Johansson, D. Misra, L. Brännholm, M. Björkhage, H. Cederquist, and H. T. Schmidt, Precision Lifetime Measurements of  $\text{He}^-$  in a Cryogenic Electrostatic Ion-Beam Trap, *Phys. Rev. Lett.* **103**, 213002 (2009).
- [21] M. Kamińska, V. T. Davis, O. M. Hole, R. F. Nascimento, K. C. Chartkunchand, M. Blom, M. Björkhage, A. Källberg, P. Löfgren, P. Reinhed, S. Rosén, A. Simonsson, R. D. Thomas, S. Mannervik, P. A. Neill, J. S. Thompson, H. T. Schmidt, H. Cederquist, and D. Hanstorp, Lifetime of the bound excited level in  $\text{Ni}^-$ , *Phys. Rev. A* **93**, 012512 (2016).
- [22] E. Bäckström, D. Hanstorp, O. M. Hole, M. Kamińska, R. F. Nascimento, M. Blom, M. Björkhage, A. Källberg, P. Löfgren, P. Reinhed, S. Rosén, A. Simonsson, R. D. Thomas, S. Mannervik, H. T. Schmidt, and H. Cederquist, Storing keV Negative Ions for an Hour: The Lifetime of the Metastable  $2^2P_{1/2}^o$  Level in  $^{32}\text{S}^-$ , *Phys. Rev. Lett.* **114**, 143003 (2015).
- [23] D. Müll, F. Grussie, K. Blaum, S. George, J. Göck, M. Grieser, R. von Hahn, Z. Harman, Á. Kálosi, C. H. Keitel, C. Krantz, C. Lyu, O. Novotný, F. Nuesslein, D. Paul, V. C. Schmidt, S. Singh, S. Sunil Kumar, X. Urbain, A. Wolf, and H. Kreckel, Metastable states of  $\text{Si}^-$  observed in a cryogenic storage ring, *Phys. Rev. A* **104**, 032811 (2021).
- [24] M. J. Jensen, U. V. Pedersen, and L. H. Andersen, Stability of the Ground State Vinylidene Anion  $\text{H}_2\text{CC}^-$ , *Phys. Rev. Lett.* **84**, 1128 (2000).
- [25] C. Breitenfeldt, K. Blaum, M. W. Froese, S. George, G. Guzmán-Ramírez, M. Lange, S. Menk, L. Schweikhard, and A. Wolf, Decay processes and radiative cooling of small anionic copper clusters, *Phys. Rev. A* **94**, 033407 (2016).
- [26] C. Breitenfeldt, K. Blaum, S. George, J. Göck, G. Guzmán-Ramírez, J. Karthein, T. Kolling, M. Lange, S. Menk, C. Meyer, J. Mohrbach, G. Niedner-Schatteburg, D. Schwalm, L. Schweikhard, and A. Wolf, Long-Term Monitoring of the Internal Energy Distribution of Isolated Cluster Systems, *Phys. Rev. Lett.* **120**, 253001 (2018).
- [27] J. N. Bull, M. S. Scholz, E. Carrascosa, M. K. Kristiansson, G. Eklund, N. Punnakayathil, N. de Ruelle, H. Zettergren, H. T. Schmidt, H. Cederquist, and M. H. Stockett, Ultraslow radiative cooling of  $\text{C}_n^-$  ( $n = 3-5$ ), *J. Chem. Phys.* **151**, 114304 (2019).
- [28] M. H. Stockett, J. N. Bull, J. T. Buntine, E. Carrascosa, E. K. Anderson, M. Gatchell, M. Kamińska, R. F. Nascimento, H. Cederquist, H. T. Schmidt, and H. Zettergren, Radiative cooling of carbon cluster anions  $\text{C}_{2n+1}^-$  ( $n = 3-5$ ), *Eur. Phys. J. D* **74**, 150 (2020).
- [29] A. P. Rasmussen, R. Teiwes, D. A. Farkhutdinova, A. V. Bochenkova, and L. H. Andersen, On the temperature of large biomolecules in ion-storage rings, *Eur. Phys. J. D* **76**, 76 (2022).
- [30] U. Hechtfisher, J. Rostas, M. Lange, J. Linkemann, D. Schwalm, R. Wester, A. Wolf, and D. Zajfman, Photodissociation spectroscopy of stored  $\text{CH}^+$  and  $\text{CD}^+$  ions: Analysis of the  $b^3\Sigma^- - a^3\Pi$  system, *J. Chem. Phys.* **127**, 204304 (2007).
- [31] C. Meyer, A. Becker, K. Blaum, C. Breitenfeldt, S. George, J. Göck, M. Grieser, F. Grussie, E. A. Guerin, R. von Hahn, P. Herwig, C. Krantz, H. Kreckel, J. Lion, S. Lohmann, P. M. Mishra, O. Novotný, A. P. O'Connor, R. Repnow, S. Saurabh *et al.*, Radiative Rotational Lifetimes and State-Resolved Relative Detachment Cross Sections from Photodetachment Thermom-

- etry of Molecular Anions in a Cryogenic Storage Ring, *Phys. Rev. Lett.* **119**, 023202 (2017).
- [32] H. T. Schmidt, G. Eklund, K. C. Chartkunchand, E. K. Anderson, M. Kamińska, N. de Ruelle, R. D. Thomas, M. K. Kristiansson, M. Gatchell, P. Reinhed, S. Rosén, A. Simonsson, A. Källberg, P. Löfgren, S. Mannervik, H. Zettergren, and H. Cederquist, Rotationally Cold OH<sup>-</sup> Ions in the Cryogenic Electrostatic Ion-Beam Storage Ring DESIREE, *Phys. Rev. Lett.* **119**, 073001 (2017).
- [33] H. T. Schmidt, G. Eklund, K. C. Chartkunchand, E. K. Anderson, M. Kamińska, N. de Ruelle, R. D. Thomas, M. K. Kristiansson, M. Gatchell, P. Reinhed, S. Rosén, A. Simonsson, A. Källberg, P. Löfgren, S. Mannervik, H. Zettergren, and H. Cederquist, Erratum: Rotationally Cold OH<sup>-</sup> Ions in the Cryogenic Electrostatic Ion-Beam Storage Ring DESIREE [Phys. Rev. Lett. **119**, 073001 (2017)], *Phys. Rev. Lett.* **121**, 079901 (2018).
- [34] U. Hechtfischer, C. J. Williams, M. Lange, J. Linkemann, D. Schwalm, R. Wester, A. Wolf, and D. Zajfman, Photodissociation spectroscopy of stored CH<sup>+</sup> ions: Detection, assignment, and close-coupled modeling of near-threshold Feshbach resonances, *J. Chem. Phys.* **117**, 8754 (2002).
- [35] D. Gerlich, Inhomogeneous rf-fields—A versatile tool for the study of processes with slow ions, *Adv. Chem. Phys.* **82**, 1 (1992).
- [36] J. U. Andersen, P. Hvelplund, S. B. Nielsen, S. Tomita, H. Wahlgreen, S. P. Møller, U. V. Pedersen, J. S. Forster, and T. J. D. Jørgensen, The combination of an electrospray ion source and an electrostatic storage ring for lifetime and spectroscopy experiments on biomolecules, *Rev. Sci. Instrum.* **73**, 1284 (2002).
- [37] A. Svendsen, H. V. Kiefer, H. B. Pedersen, A. V. Bochenkova, and L. H. Andersen, Origin of the intrinsic fluorescence of the green fluorescent protein, *J. Am. Chem. Soc.* **139**, 8766 (2017).
- [38] H. V. Kiefer, E. Gruber, J. Langeland, P. A. Kusocek, Anastasia V. Bochenkova, and L. H. Andersen, Intrinsic photoisomerization dynamics of protonated Schiff-base retinal, *Nat. Commun.* **10**, 1210 (2019).
- [39] E. Gruber, C. Kjær, S. B. Nielsen, and L. H. Andersen, Intrinsic photophysics of light-harvesting charge-tagged chlorophyll a and b pigments, *Chem. Eur. J.* **25**, 9153 (2019).
- [40] A. Wolf, H. Kreckel, L. Lammich, D. Strasser, J. Mikosch, J. Glosík, R. Plašil, S. Altevogt, V. Andrianarijaona, H. Buhr, J. Hoffmann, M. Lestinsky, I. Nevo, S. Novotny, D. A. Orlov, H. B. Pedersen, A. S. Terekhov, J. Toker, R. Wester, D. Gerlich *et al.*, Effects of molecular rotation in low-energy electron collisions of H<sub>3</sub><sup>+</sup>, *Philos. Trans. R. Soc. Lond.* **364**, 2981 (2006).
- [41] S. Menk, P. Bertier, Y. Enomoto, T. Masunaga, T. Majima, Y. Nakano, and T. Azuma, A cryogenic linear ion trap beamline for providing keV ion bunches, *Rev. Sci. Instrum.* **89**, 113110 (2018).
- [42] N. de Ruelle, M. Wolf, L. Giacomozzi, J. D. Alexander, M. Gatchell, M. H. Stockett, N. Haag, H. Zettergren, H. T. Schmidt, and H. Cederquist, DESIREE electrospray ion source test bench and setup for collision induced dissociation experiments, *Rev. Sci. Instrum.* **89**, 075102 (2018).
- [43] J. Mikosch, U. Frühling, S. Trippel, R. Otto, P. Hlavenka, D. Schwalm, M. Weidemüller, and R. Wester, Evaporation of trapped anions studied with a 22-pole ion trap in tandem time-of-flight configuration, *Phys. Rev. A* **78**, 023402 (2008).
- [44] O. Asvany and S. Schlemmer, Numerical simulations of kinetic ion temperature in a cryogenic linear multipole trap, *Int. J. Mass Spectrom.* **279**, 147 (2009).
- [45] O. Asvany, S. Brünken, L. Kluge, and S. Schlemmer, Coltrap: A 22-pole ion trapping machine for spectroscopy at 4 K, *Appl. Phys. B* **114**, 203 (2014).
- [46] O. Asvany and S. Schlemmer, Rotational action spectroscopy of trapped molecular ions, *Phys. Chem. Chem. Phys.* **23**, 26602 (2021).
- [47] J. Mikosch, H. Kreckel, R. Wester, R. Plašil, J. Glosík, D. Gerlich, D. Schwalm, and A. Wolf, Action spectroscopy and temperature diagnostics of H<sub>3</sub><sup>+</sup> by chemical probing, *J. Chem. Phys.* **121**, 11030 (2004).
- [48] O. Asvany, E. Hugo, F. Müller, F. Kühnemann, S. Schiller, J. Tennyson, and S. Schlemmer, Overtone spectroscopy of H<sub>2</sub>D<sup>+</sup> and D<sub>2</sub>H<sup>+</sup> using laser induced reactions, *J. Chem. Phys.* **127**, 154317 (2007).
- [49] O. Asvany, O. Ricken, H. S. P. Müller, M. C. Wiedner, T. F. Giesen, and S. Schlemmer, High-Resolution Rotational Spectroscopy in a Cold Ion Trap: H<sub>2</sub>D<sup>+</sup> and D<sub>2</sub>H<sup>+</sup>, *Phys. Rev. Lett.* **100**, 233004 (2008).
- [50] P. Jusko, O. Asvany, A.-C. Wallerstein, S. Brünken, and S. Schlemmer, Two-Photon Rotational Action Spectroscopy of Cold OH<sup>-</sup> at 1 ppb Accuracy, *Phys. Rev. Lett.* **112**, 253005 (2014).
- [51] R. Otto, A. von Zastrow, T. Best, and R. Wester, Internal state thermometry of cold trapped molecular anions, *Phys. Chem. Chem. Phys.* **15**, 612 (2013).
- [52] D. Hauser, S. Lee, F. Carelli, S. Spieler, O. Lakhmanskaya, E. S. Endres, S. S. Kumar, F. Gianturco, and R. Wester, Rotational state-changing cold collisions of hydroxyl ions with helium, *Nat. Phys.* **11**, 467 (2015).
- [53] E. S. Endres, G. Egger, S. Lee, O. Lakhmanskaya, M. Simpson, and R. Wester, Incomplete rotational cooling in a 22-pole ion trap, *J. Mol. Spectrosc.* **332**, 134 (2017).
- [54] H. H. Andersen and P. Tykesson, A pig sputter source for negative ions, *Nuclear Sci. IEEE Trans. on* **22**, 1632 (1975).
- [55] P. A. Schulz, R. D. Mead, P. L. Jones, and W. C. Lineberger, OH<sup>-</sup> and OD<sup>-</sup> threshold photodetachment, *J. Chem. Phys.* **77**, 1153 (1982).
- [56] J. P. Maillard, J. Chauville, and A. W. Mantz, High-resolution emission spectrum of OH in an oxyacetylene flame from 3.7 to 0.9  $\mu$ m, *J. Mol. Spectrosc.* **63**, 120 (1976).
- [57] E. Hill and J. H. Van Vleck, On the quantum mechanics of the rotational distortion of multiplets in molecular spectra, *Phys. Rev.* **32**, 250 (1928).
- [58] S. Gewurtz, H. Lew, and P. Flainek, The electronic spectrum of HF<sup>+</sup>, *Can. J. Phys.* **53**, 1097 (1975).
- [59] H. Hotop, T. A. Patterson, and W. C. Lineberger, High resolution photodetachment study of OH<sup>-</sup> and OD<sup>-</sup> in the threshold region 7000–6450 Å, *J. Chem. Phys.* **60**, 1806 (1974).
- [60] F. Breyer, P. Frey, and H. Hotop, High resolution photoelectron spectrometry of negative ions: Rotational transitions in laser-photodetachment of OH<sup>-</sup>, SH<sup>-</sup>, SD<sup>-</sup>, *Z. Phys. A* **300**, 7 (1981).
- [61] P. A. Schulz, Roy D. Mead, and W. C. Lineberger, Rotational intensities in photodetachment and photoionization, *Phys. Rev. A* **27**, 2229 (1983).
- [62] J. R. Smith, J. B. Kim, and W. C. Lineberger, High-resolution threshold photodetachment spectroscopy of OH<sup>-</sup>, *Phys. Rev. A* **55**, 2036 (1997).

- [63] J. D. Rudmin, L. P. Ratliff, J. N. Yukich, and D. J. Larson, Structure of the photodetachment cross section in a magnetic field: An experiment with  $\text{OH}^-$ , *J. Phys. B: At. Mol. Opt. Phys.* **29**, L881 (1996).
- [64] F. Goldfarb, C. Drag, W. Chaibi, S. Kröger, C. Blondel, and C. Delsart, Photodetachment microscopy of the P, Q, and R branches of the  $\text{OH}^-$  ( $v=0$ ) to  $\text{OH}$  ( $v=0$ ) detachment threshold, *J. Chem. Phys.* **122**, 014308 (2005).
- [65] P. C. Engelking, Strong electron-dipole coupling in photodetachment of molecular negative ions: Anomalous rotational thresholds, *Phys. Rev. A* **26**, 740 (1982).
- [66] Computational Chemistry Comparison and Benchmark Database, Experimental Polarizabilities, <https://cccbdb.nist.gov/pollistx.asp#1997Oln/Can:59>.
- [67] J. D. Jackson, *Classical Electrodynamics* (John Wiley & Sons, New York, 1975).
- [68] A. Svendsen, K. M. E. Nielsen, and H. B. Pedersen, Trapping ions from a fast beam in a radio-frequency ion trap: The relaxation of the ion cloud and its resulting column density, *Phys. Rev. A* **89**, 063410 (2014).
- [69] B. B. Shen, Y. Benitez, K. G. Lunny, and R. E. Continetti, Internal energy dependence of the photodissociation dynamics of  $\text{O}_3^-$  using cryogenic photoelectron-photofragment coincidence spectroscopy, *J. Chem. Phys.* **147**, 094307 (2017).
- [70] A. Svendsen, L. Lammich, J. E. Andersen, H. K. Bechtold, E. Søndergaard, F. Mikkelsen, and H. B. Pedersen, Trapping ions from a fast beam in a radio-frequency ion trap: Exploring the energy exchange with the longitudinal radio-frequency field, *Phys. Rev. A* **87**, 043410 (2013).
- [71] J. Fedor, K. Hansen, J. U. Andersen, and P. Hvelplund, Non-thermal Power Law Decay of Metal Dimer Anions, *Phys. Rev. Lett.* **94**, 113201 (2005).
- [72] S. Martin, J. Bernard, R. Brédy, B. Concina, C. Joblin, M. Ji, C. Ortega, and L. Chen, Fast Radiative Cooling of Anthracene Observed in a Compact Electrostatic Storage Ring, *Phys. Rev. Lett.* **110**, 063003 (2013).
- [73] M. Saito, H. Kubota, K. Yamasa, K. Suzuki, T. Majima, and H. Tsuchida, Direct measurement of recurrent fluorescence emission from naphthalene ions, *Phys. Rev. A* **102**, 012820 (2020).
- [74] N. Kono, R. Suzuki, T. Furukawa, J. Matsumoto, H. Tanuma, H. Shiromaru, T. Azuma, and K. Hansen, Electronic and vibrational radiative cooling of the small carbon clusters  $\text{C}_4^-$  and  $\text{C}_6^-$ , *Phys. Rev. A* **98**, 063434 (2018).
- [75] V. Chandrasekaran, B. Kafle, A. Prabhakaran, O. Heber, M. Rappaport, H. Rubinstein, D. Schwalm, Y. Toker, and D. Zajfman, Determination of absolute recurrent fluorescence rate coefficients for  $\text{C}_6^-$ , *J. Phys. Chem. Lett.* **5**, 4078 (2014).
- [76] T. R. Rizzo and O. V. Boyarkin, Cryogenic methods for the spectroscopy of large, biomolecular ions, in *Gas-Phase IR Spectroscopy and Structure of Biological Molecules*, edited by A. M. Rijs and J. Oomens (Springer International Publishing, Cham, 2015), pp. 43–97.